



Beibei Wang, Qinyi Xu,  
Chen Chen, Feng Zhang,  
and K.J. Ray Liu

# The Promise of Radio Analytics

*A future paradigm  
for wireless positioning,  
tracking, and sensing*

**W**ith the proliferation of Internet of Things (IoT) applications, billions of household appliances, phones, smart devices, security systems, environment sensors, vehicles, buildings, and other radio-connected devices will transmit data and communicate with each other or people, and it will be possible to constantly measure and track virtually everything. Among the various approaches to measuring what is happening in the surrounding environment, wireless sensing has received increasing attention in recent years because of the ubiquitous deployment of wireless radio devices. In addition, human activities affect wireless signal propagation, so understanding and analyzing how these signals react to human activities can reveal rich information about the activities around us.

As more bandwidth becomes available in the new generation of wireless systems, wireless sensing will, in the

near future, facilitate many smart IoT applications that are only imagined today. This is because, when the bandwidth increases, one can see many more multipaths in a rich-scattering environment, such as indoors or in metropolitan areas, that can be treated as hundreds of virtual antennas and/or sensors.

To control the virtual antennas and make good use of the multipaths, one can resort to the physical principles of radio propagation. Inspired by the high-resolution spatial-temporal resonance of the time reversal (TR) phenomenon, one can develop various types of radio analytics based on the multipath channel profiles.

## **Introduction**

In the IoT era, people are using wireless technologies more to understand the who, what, when, where, and how of everything happening around them. Just as human activities can affect the wireless signal propagations surrounding them, information about people's activities is embedded in the signals.

Digital Object Identifier 10.1109/MSP.2018.2806300  
Date of publication: 26 April 2018

This leads us to the conclusion that we might be able to extract meaningful information through wireless sensing by analyzing various features implanted in wireless signals.

By deploying wireless transceivers indoors, macro changes due to human activities and moving objects can be derived from the wireless signals. This process can help infer the real-time location of a moving object [1]–[8], detect an event [51]–[60], and facilitate applications in manufacturing asset tracking, intelligent transportation, and home and office security systems. In addition, micro changes generated by gestures [52] and vital signals [78]–[80] can be captured without requiring people to wear any device, which is especially useful for providing assistance to the disabled and elderly people in smart home applications.

The performance of wireless sensing depends greatly on the richness of information that can be drawn from the radio signals, while the information richness is often dictated by the channel bandwidth through which the radio signals are transmitted. Because of the constrained bandwidth of the past, only a limited number of multipaths could be seen, and not much information could be revealed. But with more bandwidth available for the next generation of wireless systems, many more smart IoT applications and services appear to be possible in the near future, because richer information becomes available with a wider bandwidth. For example, with a much larger bandwidth, one can see many more multipaths indoors, which can serve as hundreds of virtual antennas and/or sensors ready to assist in many applications.

The challenge here is how to control the virtual antennas to meet our needs for smart IoT applications. We have to resort to physics to do so, and the TR phenomenon is a good starting point [37]. The TR technique treats each path of the multipath channel as a distributed virtual antenna and provides a high-resolution spatial–temporal resonance, commonly known as the *focusing effect* [38]–[40]. In physics, the TR spatial–temporal resonance can be viewed as the result of the resonance of the electromagnetic (EM) field in response to the environment [41]. When the propagation environment changes, the involved multipath signal varies correspondingly, and, consequently, the spatial–temporal resonance also changes. Inspired by the fundamental physical principle of TR, various types of analytics, referred to as *radio analytics*, that can decipher the radio waves to reveal the activities around us, based on the wireless channel state information (CSI), can be developed to enable many cutting-edge IoT applications envisioned for a long time but never achieved.

In this article, we will present the fundamental concept of radio analytics and several types of this approach for IoT applications, including indoor positioning, indoor tracking, event detection, human radio biometrics, and vital signs monitoring. We will first discuss the impact of bandwidth on the multipath CSI and the TR principles that can fully harvest the multipath CSI. Then we discuss how to achieve centimeter accuracy in wireless indoor positioning systems (IPSs) that can offer an indoor Global Positioning System (GPS)-like capability to track human or any indoor objects without any

infrastructure, as long as Wi-Fi or long-term evolution (LTE) is available.

As such an IPS relies on CSI as a fingerprint and may require recalibration because of environmental changes, we then discuss an indoor tracking system based on the statistical EM property of the spatial focusing effect to achieve decimeter accuracy without mapping and recalibration. Inspired by the TR-based IPS that maps a location with a location-specific CSI, we find that indoor wireless propagation depends highly on the various indoor events and even the presence of different people. By mapping each event and/or person to the corresponding CSI, we can construct the notion of a TR space in which one can quantify the similarity between two indoor events and/or people and perform event detection and human recognition. Since the multipath CSI is very sensitive to even subtle environmental changes, we then discuss how to utilize the CSI change pattern to detect vital signals. Finally, we will survey and discuss recent related works.

### **Multipaths: A newfound friend**

In wireless communications, when a signal emitted from a transmitter is reflected or scattered by a scatterer, an attenuated copy of the original signal is generated and reaches the receiver through a different path. The phenomenon that a signal is received by two or more paths is known as *multipath propagation*. As depicted in Figure 1(a), where each scatterer is marked by a green star, the red arrow represents the line-of-sight (LOS) path, while the blue arrows represent paths reflected and scattered by scatterers. All of the paths together form a multipath channel between the transmitter and receiver [49]. Because two or more copies of the original signal arrive at the receiver and may be added in a noncoherent way, multipaths can cause destructive interference and degrade communication performance.

However, viewed from another perspective, the scatterers in the environment act as virtual antennas and/or sensors that can be leveraged to offer some desirable outcomes. Just imagine how everyday human activities involving motion and body movements affect the wireless signal propagation around people and thus change the channel profiles and how information about these activities becomes embedded in the signals. When signals are bounced back and forth by the scatterers, multiple replicas are generated that contain enriched, meaningful information about our activities. Each of these multipaths is, in essence, a degree of freedom naturally existing in our surrounding environment. They can be considered to be tens or hundreds of virtual antennas ready to serve us on demand.

To harvest multipaths, two key components to consider are the transmission power and bandwidth [42], [43]. On the one hand, increasing the transmission power leads to a higher signal-to-noise ratio and thus to more observable multipath components. On the other hand, the transmission bandwidth determines the spatial resolution in resolving independent multipath components. Because of the limited bandwidth, which is equal to the channel sampling rate, the multipaths with a propagation delay difference less than a channel sampling

period  $T_{\text{sample}}$  will merge into a single tap (more details are discussed in the section “Mapping-Free Indoor Tracking with Decimeter Accuracy”). Thus, as noted in Figure 1(a), the resolution to separate radio paths with different lengths in a multipath propagation is limited to  $cT_{\text{sample}} = c/B$ , with  $c$  being the speed of light and  $B$  the bandwidth. Therefore, the larger the bandwidth, the better the spatial resolution and thus the more multipaths that can be resolved. An example of multipath channel profiles captured under different bandwidths from LTE, Wi-Fi, and the entire industrial, scientific, and medical (ISM) 5-GHz band at the same location in a rich-scattering

environment is demonstrated in Figure 2. When the bandwidth is 20 MHz (as in LTE), only five multipaths can be resolved; when it increases to 40 MHz (as in Wi-Fi) approximately ten multipaths can be resolved. When it rises further, to 125 MHz, around 30 multipaths with clear details of differences can be resolved, which shows that the number of multipaths increases as the bandwidth expands.

To utilize the multipaths as virtual antennas and/or sensors, we find that a good starting point is to resort to the physics of TR and its focusing effect. In TR, with two transceivers A and B, transceiver B first sends a channel-probing signal (e.g., an

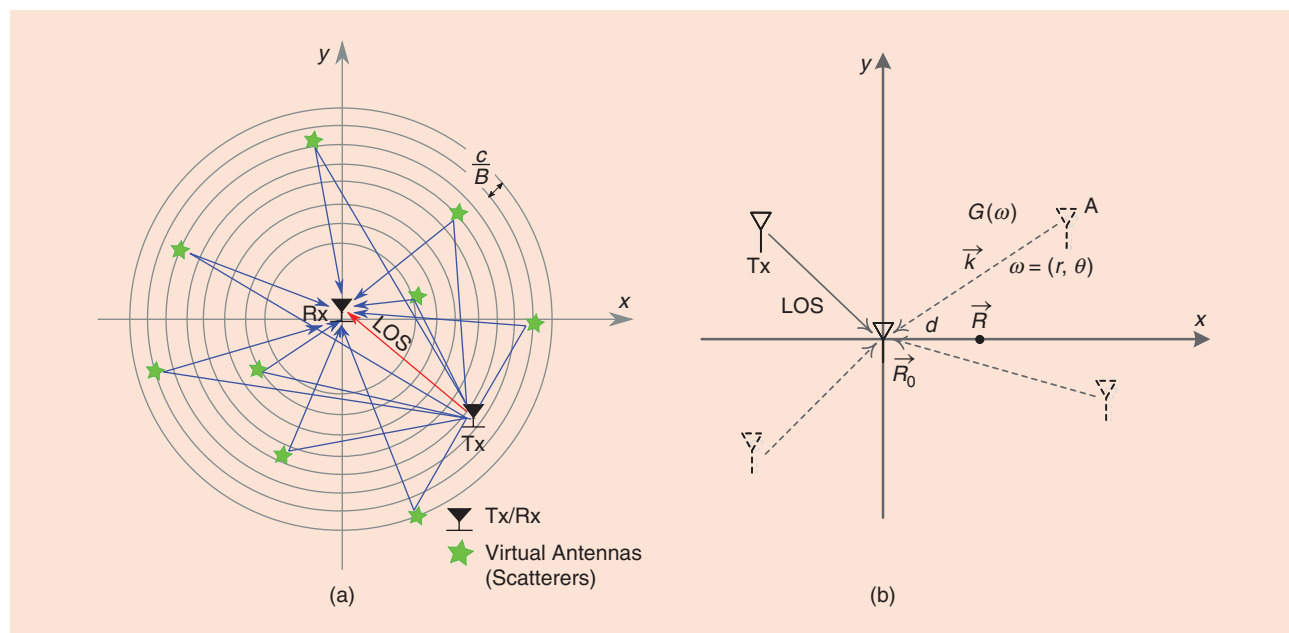


**FIGURE 1.** The concept of multipath propagation. (a) An illustration of a multipath as a virtual antenna. (b) A detailed illustration with each multipath represented by its total travel distance, direction of arrival, and power gain. Tx: transmitter; Rx: receiver.

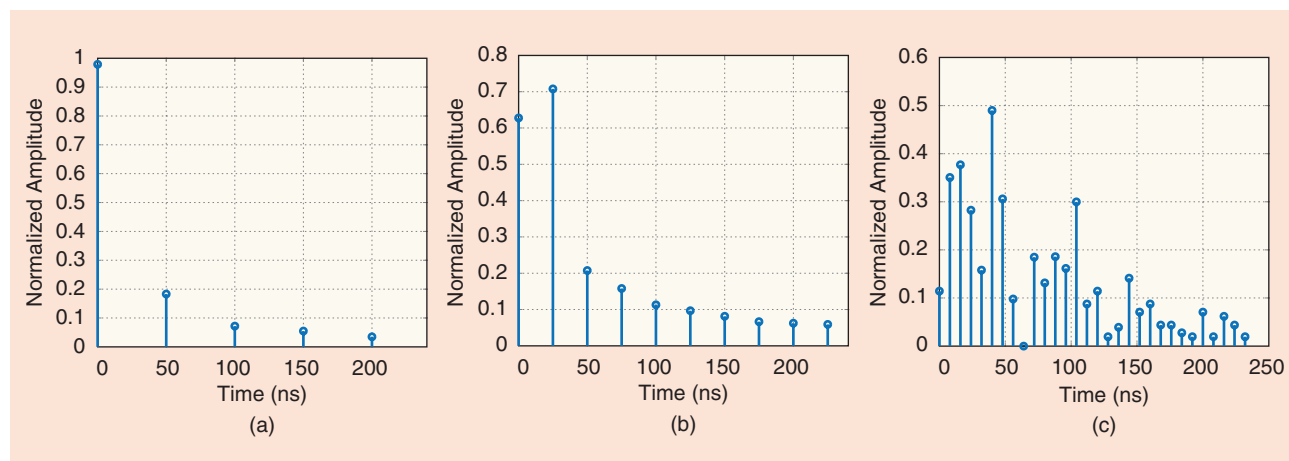


**FIGURE 2.** An illustration of multipath channel versus bandwidth. (a) The measured channel under a 20-MHz bandwidth (LTE standard). (b) The measured channel under a 40-MHz bandwidth (the IEEE 802.11n standard). (c) The measured channel under a 125-MHz bandwidth (the entire ISM 5-GHz band) [50]. We first measure a sample channel impulse response (CIR) in a typical indoor environment using a TR prototype [35] with a bandwidth of 125 MHz in the ISM 5-GHz band, and then different filters with bandwidths of 20 MHz, 40 MHz, and 125 MHz, respectively, are applied to the measured channel profile. For a linear time-invariant system, the filtering operation on the receiver side is equivalent to that on the transmitter side. Therefore, the filtered CIR is equivalent to that measured with the same bandwidth as the filter.

impulse) to transceiver A, at which the multipath CSI [44] can be estimated. Then transceiver A time-reverses the received waveform (and conjugates it, if the signal is complex) and transmits the time-reversed version of the waveform back to transceiver B. The work in [40] and [42] has shown that the convolution of the time-reversed waveform and the channel can generate a unique peak at the specific receiver's location, called the *spatial focusing effect*. This indicates that the multipath channel profile works as a unique and location-specific signature and that the spatial focusing effect happens only when the channel can match the time-reversed waveform. By comparing the multipath CSI with a set of time-reversed CSI values precollected at multiple known locations, one can infer the current location of a device, and this idea can be applied to assist positioning.

Since each multipath profile is, in essence, a focusing point on the TR logical space, if there is an event that affects the multipath, such as a door opening or closing, the multipath profile becomes mapped to another focusing point. If one can perform analytics or machine learning to distinguish both events, then one is able to infer what has happened. With this notion, we can further design various types of radio analytics based on the multipath CSI. By fully exploiting the rich multipath CSI, this approach can decipher the propagation environment as if it were a sixth human sense, revealing subtle information on various human activities. Thus, radio analytics can enable many cutting-edge IoT applications, such as accurate indoor positioning, tracking, wireless event detection, human recognition, and vital signs monitoring, as we will illustrate.

### Centimeter-accuracy indoor positioning with Wi-Fi

Today, mobile devices have become an indispensable part of daily life. To provide users with seamless services through such gadgets, it is crucial for service providers to know an individual's exact location. However, locating a person in an indoor environment is quite challenging, because signals are attenuated by the numerous multipaths in the rich-scattering indoor environment.

Most existing IPSs can achieve only meter-level accuracy, and performance becomes even worse in the non-LOS (NLOS) condition. The main reason is that it is generally difficult or even impossible to obtain precise measurements because of the rich-scattering indoor environment, and such imprecise measurements lead to ambiguity when running positioning algorithms. To reduce ambiguity, one can collect more online measurements and/or deploy multiple access points (APs), but this will increase the overhead and infrastructure cost.

As a different approach, Wu et al. developed a single-AP indoor positioning algorithm that could achieve centimeter-level accuracy with a single realization of online measurement by utilizing the TR technique [30]. Since TR is able to focus the energy of the transmitted signal only onto the intended location, by utilizing a unique, location-specific CSI, the TRIPS [30] can position a user by matching the CSI with the geographical location [37]. Since spatial focusing is a half-wavelength focus spot, the TRIPS can achieve a 1- to 2-cm level positioning

accuracy, even with a single AP working in the NLOS condition. However, TRIPS implementation requires a large bandwidth and specialized hardware. One would naturally ask if we can simply use off-the-shelf Wi-Fi to accomplish this. In this section, therefore, we discuss a centimeter-accuracy IPS using commercial Wi-Fi, where we utilize a radio analytics based on a combination of the CSI values from different frequency bands or antenna links.

### Impact of effective bandwidth

As discussed earlier, a large bandwidth is indispensable for resolving multipath CSI and high correlation of CSI values from different locations, because insufficient bandwidth can result in positioning ambiguity. To understand how bandwidth affects the accuracy of indoor positioning, we conducted extensive experiments in a typical indoor space. We deployed two channel sounders under an NLOS setting, with one of them placed on an experimental structure with a 5-mm measurement resolution. At each location of the experimental structure, we collected multiple CSI values as location-specific fingerprints under different bandwidths. To assess the similarities among locations, we defined an analytic value of the CSI values belonging to two locations—the TR resonating strength (TRRS) [31]—as

$$\mathcal{TR}(\mathbf{h}_{F,1}, \mathbf{h}_{F,2}) = \left( \frac{\eta}{\sqrt{\Lambda_1} \sqrt{\Lambda_2}} \right)^2, \quad (1)$$

with  $\eta = \max_{\phi} \left| \sum_{k=1}^{N_{\text{sub}}} h_{F,1}[k] h_{F,2}[k]^* e^{-jk\phi} \right|$ ,  $\Lambda_1 = \sum_{k=1}^{N_{\text{sub}}} |h_{F,1}[k]|^2$ , and  $\Lambda_2 = \sum_{k=1}^{N_{\text{sub}}} |h_{F,2}[k]|^2$ , where  $\mathbf{h}_{F,1}$  and  $\mathbf{h}_{F,2}$  represent two CSI vectors in the frequency domain [i.e., the channel frequency response (CFR)],  $N_{\text{sub}}$  stands for the number of usable subcarriers,  $h_{F,1}[k]$  and  $h_{F,2}[k]$  are the CFRs on subcarrier  $k$ ,  $\eta$  is the modified cross correlation between  $\mathbf{h}_{F,1}$  and  $\mathbf{h}_{F,2}$  after compensating for the phase distortions caused by synchronization errors, and  $\Lambda_1, \Lambda_2$  are the CFR energies with respect to  $\mathbf{h}_{F,1}$  and  $\mathbf{h}_{F,2}$ .

The experimental results in Figure 3 illustrate the TRRS distribution among the central location on the experimental structure and its nearby locations under different effective bandwidths. The figure shows that 40 MHz of bandwidth is insufficient to distinguish nearby locations centimeters away. The ambiguity decreases significantly with an increasing bandwidth. When the effective bandwidth reaches 360 MHz, the region of ambiguity shrinks to a ball with an approximately 1-cm radius, which indicates centimeter-level accuracy.

Unfortunately, the bandwidths on mainstream 802.11n Wi-Fi chips are merely 20 or 40 MHz, insufficient for centimeter-level indoor positioning. This motivates the formulation of a large effective bandwidth by exploiting the diversities on Wi-Fi devices, i.e., the frequency and spatial diversity.

Figure 4 shows a generalized framework of diversity exploitation. More specifically, Figure 4(a) shows an example of fusing CSI values from four different Wi-Fi channels, while Figure 4(b) demonstrates merging the CSI values from four receiving antennas. Both diversities can be exploited at the

same time, as shown in Figure 4(c), where the CSIs on two Wi-Fi channels and two receiving antennas are combined into one fingerprint. In Wi-Fi, the frequency diversity is achieved by performing frequency hopping on different Wi-Fi channels [32], and the spatial diversity can be realized by collecting CSI on multiple antenna links on multiple-input, multiple-output (MIMO) Wi-Fi devices [33]. When we denote the maximum frequency diversity by  $F$ , the maximum spatial diversity by  $S$ , and the physical bandwidth for each Wi-Fi channel by  $B$ , the effective bandwidth is given as  $S \times F \times B$ . Diversity exploitation increases the effective bandwidth to  $S \times F$  times compared to the physical bandwidth  $B$ .

### Achieving centimeter accuracy via TRRS

For Wi-Fi devices with a spatial diversity of  $S$  and a frequency diversity of  $F$ , the collected CSI values can be written as

$$\bar{\mathbf{H}}_F = \{\mathbf{h}_F^{(s,f)}\}_{s=1,2,\dots,S}^{f=1,2,\dots,F},$$

where  $\mathbf{h}_F^{(s,f)}$  stands for the CSI obtained on the  $s$ th antenna link on the  $f$ th Wi-Fi channel. This expression provides a fine-grained fingerprint with an effective bandwidth of  $S \times F \times B$ . Thus, the TRRS in (1) could be extended to the fine-grained fingerprint  $\bar{\mathbf{H}}_{F,1}$  and  $\bar{\mathbf{H}}_{F,2}$ , with

$$\eta = \sum_{s=1}^S \sum_{f=1}^F \eta^{(s,f)}, \quad \Lambda_1 = \sum_{s=1}^S \sum_{f=1}^F \Lambda_1^{(s,f)},$$

and

$$\Lambda_2 = \sum_{s=1}^S \sum_{f=1}^F \Lambda_2^{(s,f)},$$

where

$$\eta^{(s,f)} = \max_{\phi} \left| \sum_{k=1}^K h_{F,1}^{(s,f)}[k] h_{F,2}^{(s,f)*}[k] e^{-jk\phi} \right|$$

is the modified cross correlation on  $(s,f)$ , and

$$\Lambda_1^{(s,f)} = \sum_{k=1}^{N_{\text{sub}}} |h_{F,1}^{(s,f)}[k]|^2, \quad \Lambda_2^{(s,f)} = \sum_{k=1}^{N_{\text{sub}}} |h_{F,2}^{(s,f)}[k]|^2$$

are the CSI energies of  $\mathbf{h}_{F,1}^{(s,f)}$  and  $\mathbf{h}_{F,2}^{(s,f)}$  on  $(s,f)$ , respectively. Then, the fused TRRS  $\mathcal{TR}(\bar{\mathbf{H}}_{F,1}, \bar{\mathbf{H}}_{F,2})$  calculated by (1) implies that it is a weighted average of CSI energies on different Wi-Fi channels and antenna links.

Treating the CSI as a location-specific fingerprint and the TRRS as the classification metric, we discuss an IPS that consists of an offline phase and an online one in the following. During the offline phase, the positioning system collects CSI fingerprints from  $N_{\text{loc}}$  locations of interest, denoted as  $\{\bar{\mathbf{H}}_{F,\ell}\}_{\ell=1,2,\dots,N_{\text{loc}}}$ . In the online phase, a CSI fingerprint  $\bar{\mathbf{H}}_{F,\text{test}}$  is obtained at a location

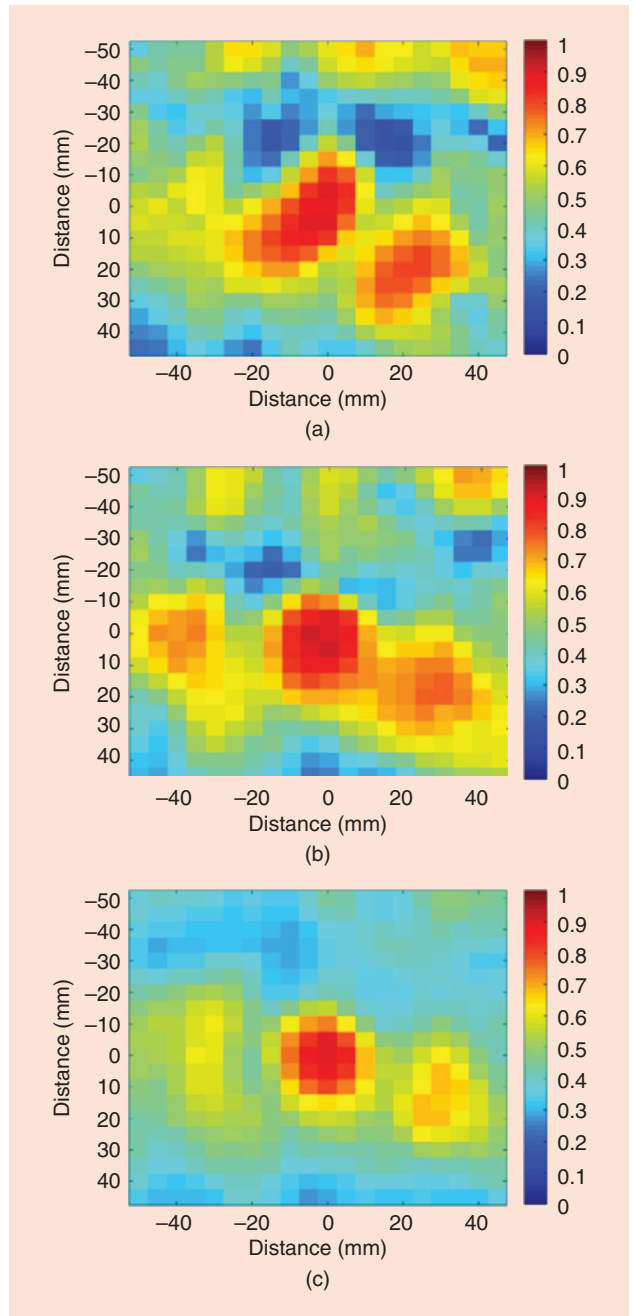


**FIGURE 3.** The ambiguity among nearby locations under (a) a 40-MHz effective bandwidth, (b) a 120-MHz effective bandwidth, and (c) a 360-MHz effective bandwidth.

to be determined, which may be either one out of the  $N_{\text{loc}}$  locations of interest mapped during the online phase or an unmapped location. Then, the pairwise TRRS between the fingerprint  $\bar{\mathbf{H}}_{F,\text{test}}$  and each of the  $N_{\text{loc}}$  fingerprints  $\{\bar{\mathbf{H}}_{F,\ell}\}_{\ell=1,2,\dots,N_{\text{loc}}}$  is computed as  $\mathcal{TR}(\bar{\mathbf{H}}_{F,\ell}, \bar{\mathbf{H}}_{F,\text{test}})$ . Finally, the location is determined based upon  $\mathcal{TR}(\bar{\mathbf{H}}_{F,\ell}, \bar{\mathbf{H}}_{F,\text{test}})$ , as shown in (2). Here,

$$\hat{\ell} = \begin{cases} \underset{\ell=1,2,\dots,N_{\text{loc}}}{\operatorname{argmax}} \mathcal{TR}(\bar{\mathbf{H}}_{F,\ell}, \bar{\mathbf{H}}_{F,\text{test}}), & \text{If } \max_{\ell=1,2,\dots,N_{\text{loc}}} \mathcal{TR}(\bar{\mathbf{H}}_{F,\ell}, \bar{\mathbf{H}}_{F,\text{test}}) \geq \Gamma \\ 0, & \text{Otherwise} \end{cases}. \quad (2)$$

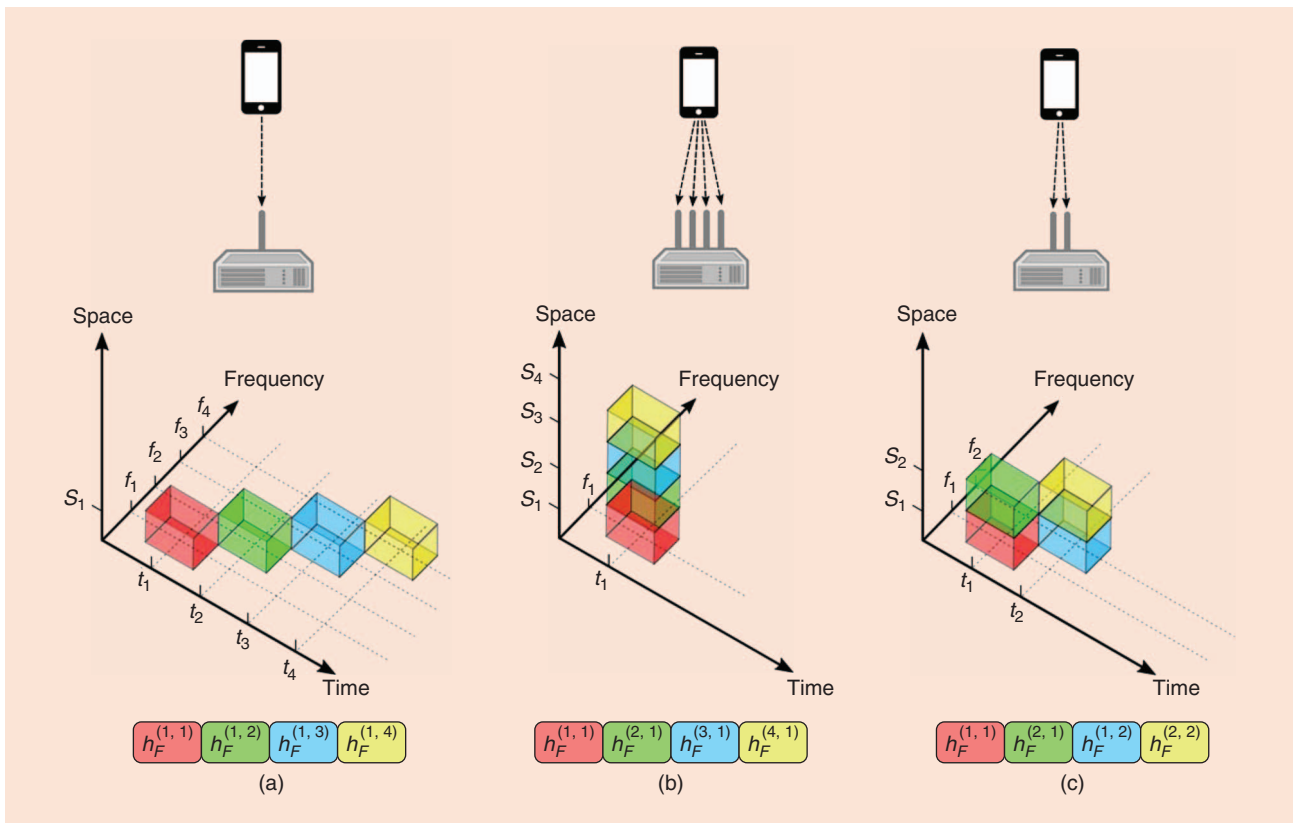


**FIGURE 4.** An illustration of leveraging frequency and spatial diversities in Wi-Fi to achieve large effective bandwidth: (a) frequency diversity, (b) spatial diversity, and (c) frequency–spatial diversity.

$\Gamma$  is a threshold to strike a balance of the true-positive rate and false-positive rate in positioning. When  $\mathcal{TR}(\hat{\mathbf{H}}_{F,\ell}, \hat{\mathbf{H}}_{F,\text{test}}) < \Gamma$ , the IPS cannot formulate a credible location estimation and thus returns zero to imply an unrecognized location.

### Experimental results

To evaluate the positioning performance in practice, we deployed two Wi-Fi devices, each equipped with three omnidirectional antennas, in an indoor office environment consisting of a large number of objects—such as chairs, desks, shelves, and sofas—as well as ceilings and walls. We measured CSI values from 50 locations of interest, with 20 CSI values for each.

We evenly divided the 20 measured CSI values at each location into a training set and a testing set. We calculated the TRRS matrix using the CSIs collected at the 50 candidate locations. Each element of the matrix represents the TRRS between the CSI values at the training and testing locations. Therefore, the block diagonal components of the TRRS matrix indicate the similarity among CSI values obtained at the same locations, while the block off-diagonal components indicate the similarity among CSI values of different locations.

Figure 5 illustrates the TRRS matrices under the effective bandwidths of 10, 40, 120, and 360 MHz. First, we see from Figure 5 that the block diagonal components of the matrices are close to 1, meaning high similarities among CSI values of the same locations, while the off-diagonal

components decrease with an increasing effective bandwidth. When the effective bandwidth is small, e.g., 10 MHz, some off-diagonal components are even greater than the diagonal ones, which leads to positioning errors. The gap between the diagonal and off-diagonal components increases as the effective bandwidth increases, resulting in improved positioning performance.

There are environmental dynamics in indoor spaces due to the movement of people and objects, and these dynamics could severely degrade the positioning performance, since they introduce random perturbations in the CSI fingerprints. However, since the proposed positioning technique exploits a large effective bandwidth from multiple antennas and/or multiple Wi-Fi channels and utilizes the entire multipath CSI signature with a high degree of freedom as a unique feature for positioning, it is robust against environmental dynamics, which can affect only a portion of the multipath propagation.

Figure 6(a) shows the receiver operating characteristic (ROC) curve with human activities, where a person walked continuously around one Wi-Fi device used for channel sounding. For a fixed false-positive rate of 0.15%, the true-positive rate increased from 94.17% at a 40-MHz effective bandwidth up to 99.11% at a 120-MHz effective bandwidth. When the effective bandwidth reached 240 MHz and then 360 MHz, the true-positive rate further increased to 99.61% and 99.89%, respectively. Figure 6(b) shows the ROC curve with large object movement, where a person operated

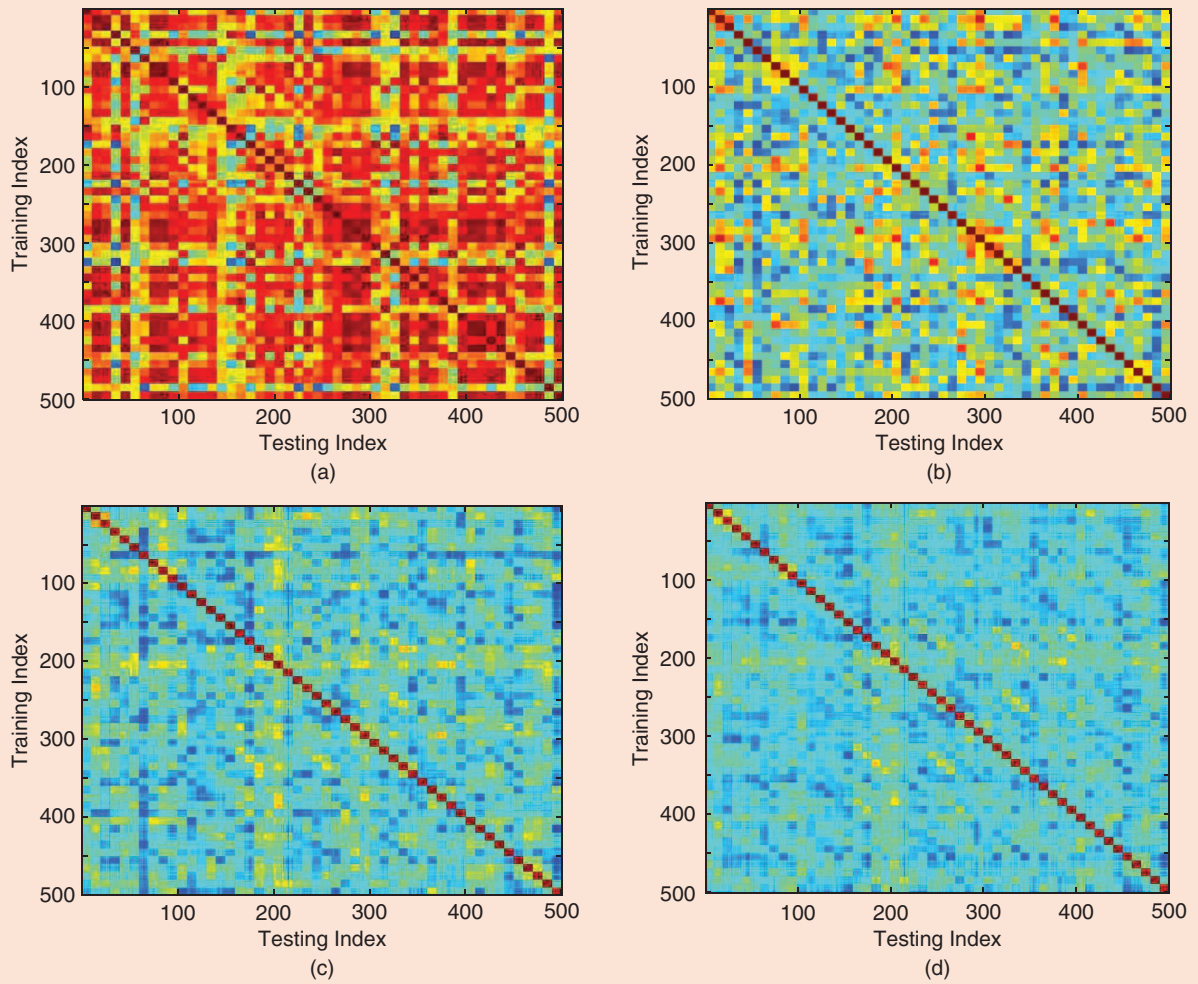


FIGURE 5. The TRRS matrix under an effective bandwidth of (a) 10 MHz, (b) 40 MHz, (c) 120 MHz, and (d) 360 MHz.

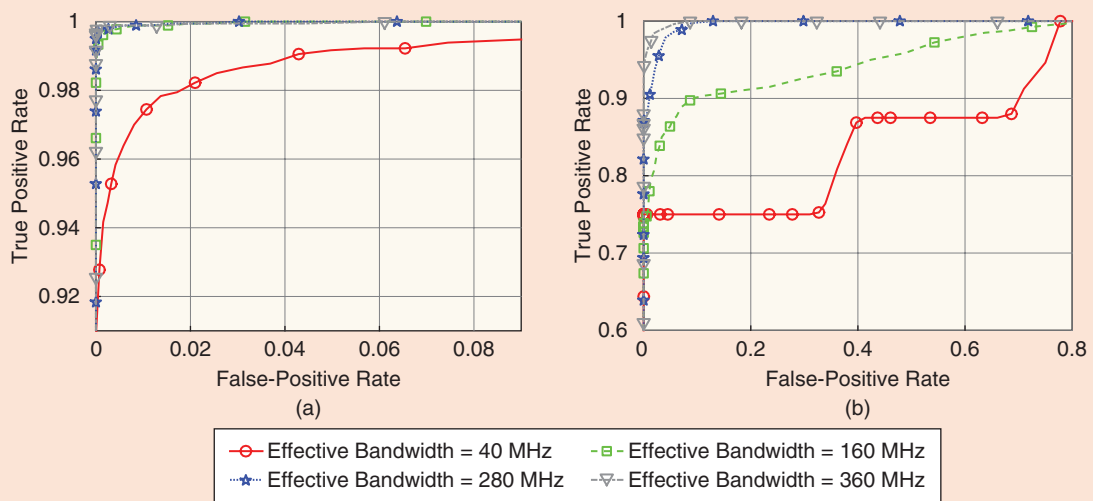


FIGURE 6. The ROC curve in the presence of environmental dynamics: (a) dynamics from human movement and (b) dynamics from large object movement [32].

a door that blocked the direct LOS path between the Wi-Fi devices. For a fixed false-positive rate of 0.15%, the true-positive rate increased from 75% at a 40-MHz effective bandwidth to 76.38%, 87.12%, and 95% at the 120-, 240-, and 360-MHz effective bandwidths, respectively. We can see from the experiment that a large effective bandwidth not only enhances the positioning accuracy but also boosts the robustness of indoor positioning against random environmental perturbations [33].

### Mapping-free indoor tracking with decimeter accuracy

The reliability of the centimeter-accuracy IPS discussed previously depends on whether the CSI fingerprints in the offline database are up to date or not. If the environmental changes affect the CSI and thus degrade the positioning accuracy, the CSI database needs to be updated, which will increase the IPS overhead. To avoid having to recalibrate the CSI fingerprints, we analyze the TRRS spatial distribution and present a mapping-free TR-based indoor tracking system (TRITS) that can achieve decimeter accuracy. As the TRITS tracks a moving object based on its previous location and current location displacement, which consists of a moving distance and a moving direction, and the moving direction can be estimated through an inertial measurement unit (IMU), we focus on the moving distance estimation. Then, we discuss a map-based position correction technology to reduce the accumulated tracking error.

#### Distance estimation based on TRRS spatial distribution

Given a large enough bandwidth, the multipaths in a rich-scattering environment can be resolved into multiple taps in discrete time. Let  $h_{T,\bar{T}-\bar{R}_0}[k]$  be the  $k$ th tap of the time-domain channel impulse response (CIR) from  $\bar{T}$  to  $\bar{R}_0$ , where  $\bar{T}$  and  $\bar{R}_0$  are the coordinates of the transmitter and receiver, respectively. Then we denote the time-reversed and conjugated version of the captured CIR as  $h_{T,\bar{R}_0-\bar{T}}^*[-k]$ , where  $*$  indicates complex conjugation. With channel reciprocity, the received signal at any location  $\bar{R}$  when the TR waveform  $h_{T,\bar{R}_0-\bar{T}}^*[-k]$  is transmitted can be written as

$$s_{\bar{R}}[k] = \sum_{l=0}^{N_{\text{tap}}-1} h_{T,\bar{T}-\bar{R}_0}[l] h_{T,\bar{R}_0-\bar{T}}^*[l-k], \quad (3)$$

where  $N_{\text{tap}}$  is the number of taps resolved in the CIR. When  $\bar{R} = \bar{R}_0$  and  $k = 0$ ,  $s_{\bar{R}}[k] = \sum_{l=0}^{N_{\text{tap}}-1} |h_{T,\bar{T}-\bar{R}_0}[l]|^2$ , with all of the multipaths added up coherently; i.e., the signal energy is refocused on the particular spatial location at a specific time instance. This phenomenon is called the *TR spatial-temporal resonating effect* [30].

To study the TR resonating effect in the spatial domain, let us fix the time index  $k = 0$  and define the TRRS between the CIRs of two locations  $\bar{R}_0$  and  $\bar{R}$  as the normalized energy of the received signal when the TR waveform for location  $\bar{R}_0$  is transmitted as shown in (4), where  $\mathbf{h}_{T,\bar{R}}$  is an abbreviation of  $h_{T,\bar{T}-\bar{R}}[l]$ ,  $l = 0, \dots, N_{\text{tap}} - 1$ , when  $\bar{T}$  is fixed.

$$\mathcal{TR}(\mathbf{h}_{T,\bar{R}_0}, \mathbf{h}_{T,\bar{R}}) = \left| \frac{s_{\bar{R}}[0]}{\sqrt{\sum_{l_1=0}^{N_{\text{tap}}-1} |h_{T,\bar{T}-\bar{R}_0}[l_1]|^2} \sqrt{\sum_{l_2=0}^{N_{\text{tap}}-1} |h_{T,\bar{T}-\bar{R}}[l_2]|^2}} \right|^2, \quad (4)$$

$$h_{T,\bar{T}-\bar{R}}(t) = \sum_{\omega \in \Omega} G(\omega) q(t - \tau(\omega)) \times e^{i(2\pi f_0(t - \tau(\omega)) - \phi(\omega) - \vec{k}(\omega) \cdot \vec{R})}, \quad (5)$$

$$h_{T,\bar{T}-\bar{R}}[l] = \sum_{\tau(\omega) \in [lT - \frac{T}{2}, lT + \frac{T}{2})} G(\omega) q(\Delta\tau(l, \omega)) \times e^{i(2\pi f_0 \Delta\tau(l, \omega) - \phi(\omega) - \vec{k}(\omega) \cdot \vec{R})}, \quad (6)$$

$$s_{\bar{R}}[0] = \sum_{l=1}^{N_{\text{tap}}} \left| \sum_{\tau \in [lT - \frac{T}{2}, lT + \frac{T}{2})} G(\omega) q(\Delta\tau(l, \omega)) \times e^{i(2\pi f_0 \Delta\tau(l, \omega) - \phi(\omega))} \right|^2. \quad (7)$$

A more detailed illustration of the multipath propagation is displayed in Figure 1(b), where each multipath is represented by the total traveled distance of the multipath  $r$ , the direction of arrival of the multipath  $\theta$ , and the power gain  $G(\omega)$ , with  $\omega = (r, \theta)$ . For any point  $\bar{R}$  in a source-free region with constant mean electric and magnetic fields, the CIR, when a delta-like pulse is transmitted, can be written as (5) [48], where  $\Omega$  is the set of multipaths,  $q(t)$  is the pulse shaper,  $\tau(\omega) = r/c$  is the propagation delay of the multipath  $\omega$ ,  $f_0$  is the carrier frequency,  $\phi(\omega)$  is the change of phase due to reflections, and  $\vec{k}(\omega)$  is the wave vector of amplitude  $k = cf_0$ . Accordingly, the  $l$ th tap of a sampled CIR at location  $\bar{R}$  can be expressed as in (6), where  $T$  is the channel measurement interval and  $\Delta\tau(l, \omega) = lT - \tau(\omega)$  for  $l = 0, 1, \dots, N_{\text{tap}} - 1$ . When the TR waveform  $h_{T,\bar{R}_0-\bar{T}}^*[-l]$  is transmitted, the corresponding received signal at the focal spot  $\bar{R}_0$  can be written as (7), which shows that the multipaths with propagation delays  $\tau(\omega) \in [lT - \frac{T}{2}, lT + \frac{T}{2})$  would be merged into the  $l$ th tap in an incoherent way, while the signals coming from different taps would add up coherently. Therefore, the larger the bandwidth, the larger the TR focusing gain that can be achieved, since more multipaths can be aligned and added up coherently. When the bandwidth is sufficiently large, the received signal at each point  $\bar{R}$  can be approximated as

$$s_{\bar{R}}[0] \approx \sum_{l=1}^{N_{\text{tap}}} |G(\omega) q(\Delta\tau(l, \omega))|^2 e^{-i\vec{k}(\omega) \cdot (\vec{R} - \vec{R}_0)}. \quad (8)$$

Without loss of generality, the energy distribution of each multipath in a rich-scattering environment can be assumed uniform in  $\theta$ ; i.e., the distribution of  $G(\omega)$  is only a function of  $r$ . Then, the energy of the multipaths coming from different directions would be approximately the same when there is a large number of them. When a rectangular pulse shaper is used, i.e.,  $q(t) = 1$  for  $t \in [-(T/2), T/2]$ , and  $q(t) = 0$  otherwise, under the above assumptions, the received signal  $s_{\bar{R}}[0]$  can be approximated as

$$\begin{aligned}
s_{\vec{R}}[0] &= \sum_{\omega \in \Omega} |G(\omega)|^2 e^{-i\vec{k} \cdot (\vec{R} - \vec{R}_0)} \\
&\approx \int_0^{2\pi} P(\theta) e^{-ikd \cos(\theta)} d\theta \\
&= PJ_0(kd),
\end{aligned} \tag{9}$$

where the coordinate system in Figure 1(b) is assumed,  $J_0(x)$  is the zeroth-order Bessel function of the first kind, and  $d$  is the Euclidean distance between  $\vec{R}_0$  and  $\vec{R}$ . Here, a continuous integral is used to approximate the discrete sum, and  $P(\theta) = P$  denotes the density of the energy of the multipaths coming from direction  $\theta$ . For  $\vec{R} = \vec{R}_0$ , it degenerates to  $d = 0$ , and thus  $s_{\vec{R}}[0] \approx P$ . Since the denominator of (4) is the product of the energy received at two focal spots, it would converge to  $P^2$ . Substituting (9) into the TRRS defined in (4) leads to

$$\mathcal{TR}(\mathbf{h}_{T,\vec{R}_0}, \mathbf{h}_{T,\vec{R}}) \approx J_0^2(kd). \tag{10}$$

Since the theoretical approximation of the TRRS distribution depends only on the distance between two points, in the following, we use  $\mathcal{TR}(d) = J_0^2(kd)$  to stand for the approximation of the TRRS between two points with distance  $d$  between them.

This theoretical analysis can be verified using a mobile channel probing platform equipped with stepping motors that can control the granularity of the CIR measurements precisely along any predefined direction. We collected extensive measurements of CIRs from different locations in a typical office environment, and Figure 7 shows two representative results measured at two locations approximately 20 m apart. In this figure, the distance  $d$  away from each predefined focal spot increases from 0 to  $2\lambda$ , with a resolution of 1 mm. It indicates that the measured TRRS distributions agree with the theoretical analysis quite well, in that the positions of the peaks and valleys in the measured curves are almost the same as those of the theoretical curves. Although the two locations are far apart, the measured TRRS distributions exhibit similar damping patterns when the distance  $d$  increases, which shows that the TRRS distribution is independent of the locations. We also see that the measured TRRS distribution curves are above the theoretical curve. This is due to the contribution of the direct path between the transmitter and receiver, which adds an asymmetric component in the energy density function  $P(\theta)$  in (9). As a result, the TRRS is a superposition of  $J_0^2(kd)$  and some unknown function. Nevertheless, since the pattern  $J_0^2(kd)$  is dominant in the TRRS distribution function and location independent, we can exploit this feature for speed estimation and then estimate the moving distance by integrating the speed over time.

Specifically, since the shape of the TRRS distribution function  $\mathcal{TR}(d) \approx J_0^2(kd)$  is determined only by the wave number  $k$ , which is dependent only on the carrier frequency and is independent of location, it can be utilized as an intrinsic ruler to measure distance. Consider that a receiver moves along a straight line with a constant speed  $v$ , starting from location  $\vec{R}_0$ , and a transmitter keeps transmitting the TR waveform

corresponding to  $\vec{R}_0$  at regular intervals. Then, the TRRS measured at the receiver is just a sampled version of  $\mathcal{TR}(d)$ , which would also exhibit the Bessel-function-like pattern, as illustrated in Figure 8. The feature points, i.e., the local peaks and valleys, on the Bessel-function-like TRRS distribution can be used to estimate the instantaneous speed of a moving object.

For example, consider the first local peak of  $\eta(d)$ , in which the theoretical distance  $d_1$  from the starting point  $\vec{R}_0$  is approximately  $0.61\lambda$ . To estimate the moving speed, we need only estimate how much time  $\hat{t}$  it takes for the receiver to reach the first local peak, starting from point  $\vec{R}_0$ . Then, the speed estimation becomes  $\hat{v} = (0.61\lambda)/\hat{t}$ . At a high sampling rate, we can assume that the actual speed within  $\hat{t}$  is constant, and then we can further estimate the moving distance by integrating the instantaneous speed over time. A more recent study [36] has shown that the speed and distance of a moving object can be estimated based on CSI from Wi-Fi with a similar accuracy, even without wearable devices. The moving direction can be estimated using IMU measurements. Combining the estimation of the moving direction and moving distance, the moving object can be tracked.

### Map-based position correction

Since the TRRS estimates the location of a moving object based on its previous location and the current location displacement,

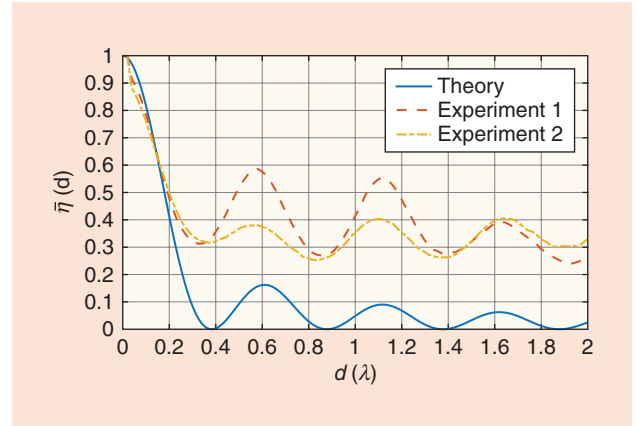


FIGURE 7. A comparison of the TRRS distribution between the experimental results and the theoretical result [36].

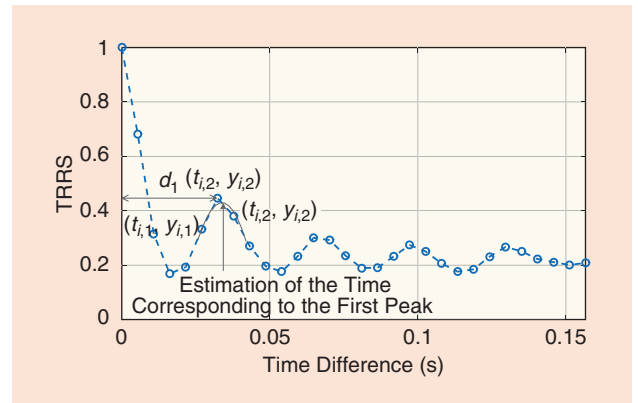


FIGURE 8. An illustration of the distance estimation method.

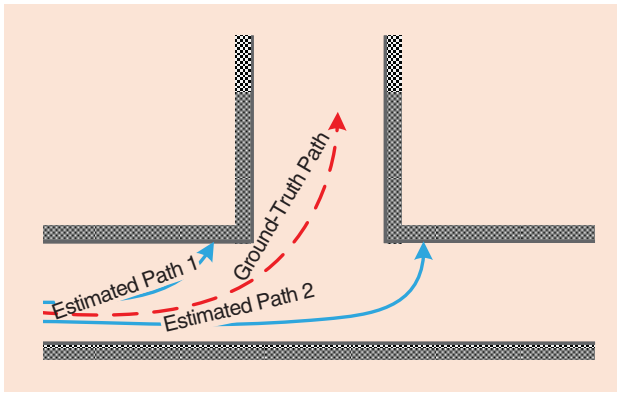


FIGURE 9. An illustration of map-based position correction.

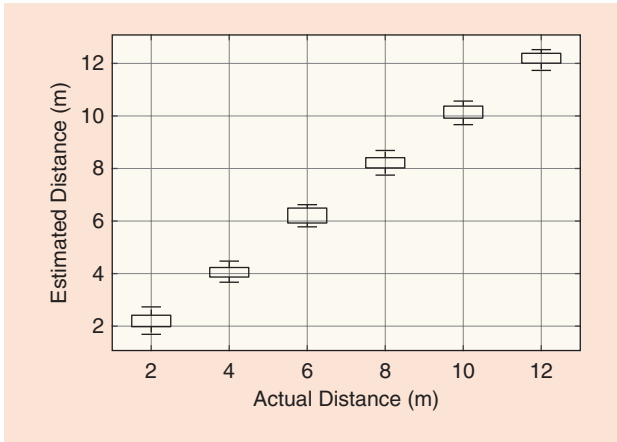


FIGURE 10. The results of walking distance estimation, with the four top-to-bottom lines in each block representing the fifth, 25th, 75th, and 95th percentiles of the estimated distance.

the positioning accuracy will be degraded by accumulated error. Nevertheless, interior structures, such as doors, walls, and corridors in the floor plan, can be embedded in the TRITS and work as constraints and landmarks to alleviate the error. For example, Figure 9 shows a T-shaped corridor with two possible estimated paths. Compared to the ground-truth trajectory denoted by the dashed line, estimated paths 1 and 2 will penetrate a wall. In these two cases, a reasoning procedure can be performed that adjusts each path so that its estimated trajectory can be fitted to the floor plan and all of the boundary constraints imposed by the floor plan can be satisfied. In this way, the accumulated error from both the distance and the direction estimation can be corrected.

### Experiments

The first set of experiments was to estimate the moving distance of a human walking inside an office. One experiment participant carried the transmitter and walked, in turn, 2, 4, 6, 8, 10, and 12 m. For each distance, we repeated the experiment 20 times along different paths; the walking speed did not need to be constant. The results are shown in Figure 10. The error in distance estimation is mainly due to the transmitter being car-

ried in the participant's hand; the trajectory is inevitably affected by the human body's movement during walking, while the distance estimator actually calculates the integration of speed over all moving directions. When the distance is shorter, the impact of this kind of error can be magnified. Nevertheless, when the walking distance is large, the impact of the uncontrollable errors on the distance estimation is insignificant.

We also evaluated the statistical distribution of the TRITS location error. In the experiment, a participant walked along a path in the same office environment, denoted by the green line in Figure 11. The person started from point A and stopped at different path locations, which are marked by green double circles. The distances from starting point A to each end point were 5, 11, 21, 25, 30, 40, 55, 64, and 69 m. For each path length, we repeated the experiment 25 times. The cumulative distribution function (CDF) of the location estimation error for all of the paths is shown in Figure 12. The median of the estimation error is around 0.33 m, and the 80th percentile is around 1 m. Therefore, the TRITS can track a moving object in a complex indoor environment at submeter accuracy.

### Wireless event detection

Inspired by the TR-based indoor positioning that associates a location with a CSI fingerprint, we can also utilize the TR technique to capture the variations in the multipath CSI due to different indoor events, such as opening or closing a door or window. By treating each path of the multipath channel in a rich-scattering environment as a distributed virtual antenna, a TR-based indoor event detection system (TRIEDS) can be designed that takes the multipath CSI as the feature and determines the occurrence of an indoor event according to the current CSI in the propagation environment.

#### CSI as a feature for event detection

The TRIEDS exploits the intrinsic property of the TR technique, i.e., capturing and fusing the information of the multipath propagation environment in the spatial resonance. To detect the occurrence of an indoor event by TR spatial resonances, the TRIEDS first learns through an offline training phase and then works in an online testing phase. Specifically, in the training phase, a training database is built by collecting the CSI, e.g., the time-domain CIR  $\mathbf{h}_T$ , from each indoor event through channel probing. After that, in the online testing phase, the TRIEDS first estimates the instantaneous multipath CSI  $\mathbf{h}_{T,\text{test}}$  from the current indoor environment and then makes the detection based on the one in the offline training database that generates the greatest strength of the generated spatial resonance.

#### Phase 1: Offline training

For each indoor event  $S_i \in \mathcal{D}$ , with  $\mathcal{D}$  being the event set, the corresponding CSI is obtained through channel probing and forms a matrix  $\mathbf{H}_{T,i}$  as  $\mathbf{H}_{T,i} = [\mathbf{h}_{T,i}(t_0), \mathbf{h}_{T,i}(t_1), \dots, \mathbf{h}_{T,i}(t_{N-1})]$ , where  $N$  is the size of the CSI samples for a training event. The vector  $\mathbf{h}_{T,i}(t_j)$  represents the estimated CSI vector of event  $S_i$  at time  $t_j$ , and  $\mathbf{H}_{T,i}$  becomes the CSI matrix for event  $S_i$ .

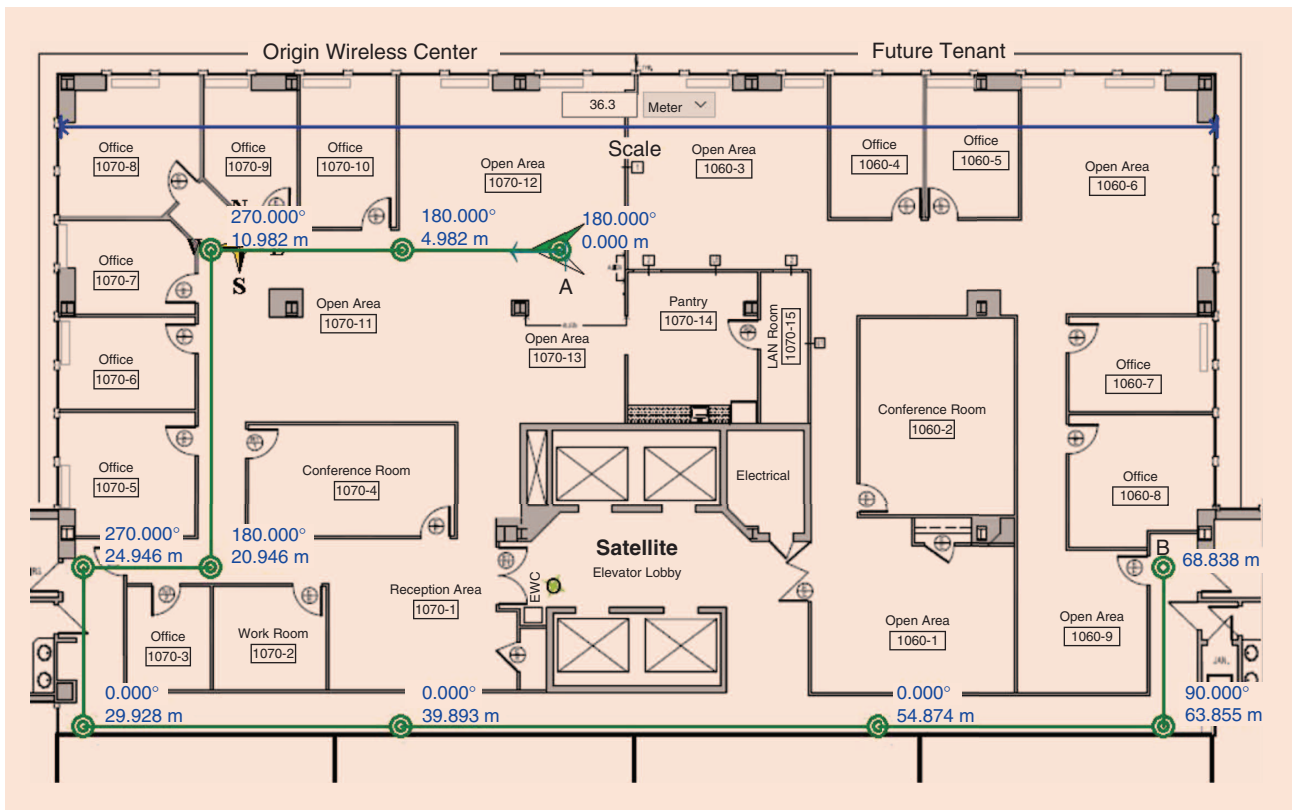


FIGURE 11. An illustration of the route and the floor plan in evaluating the statistical position error.

## Phase 2: Online testing

The objective of a TRIEDS is to detect the occurrence of each trained indoor event through evaluating the similarity between the testing and the training CSI in the training database  $\mathcal{G}$ . The raw CSI obtained from radio devices is complex-valued and of high dimensions, which complicates the detection problem and increases the computational intricacy.

With the spatial resonance effect, the TR technique provides an accurate and simple method for comparing two CSI samples. As demonstrated in Figure 13, each dot in the CSI logical space represents an indoor event or location, which is uniquely determined by the multipath profile  $\mathbf{h}$ . By taking a time-reverse and conjugate operation over the multipaths, the corresponding TR signatures  $\mathbf{g}$  are generated, and the points in the CSI logical space, as marked by A, B, and C, are mapped into the TR space, a point logical space, as points  $A'$ ,  $B'$ , and  $C'$ . In the TR space, the similarity between two indoor events or indoor locations is quantified by the TRRS. The higher the TRRS, the more similar are the two multipath profiles in the TR space. Similar events defined by a TRRS threshold will be treated as a single class in the TRIEDS.

Mathematically, the TRRS  $\mathcal{TR}(\mathbf{h}_{T,1}, \mathbf{h}_{T,2})$  between two CIRs  $\mathbf{h}_{T,1}$  and  $\mathbf{h}_{T,2}$  is defined as

$$\mathcal{TR}(\mathbf{h}_{T,1}, \mathbf{h}_{T,2}) = \left( \frac{\max_i |(\mathbf{h}_{T,1} * \mathbf{g}_{T,2})[i]|}{\sqrt{\sum_{l=0}^{N_{\text{tap}}-1} |h_{T,1}[l]|^2} \sqrt{\sum_{l=0}^{N_{\text{tap}}-1} |h_{T,2}[l]|^2}} \right)^2, \quad (11)$$

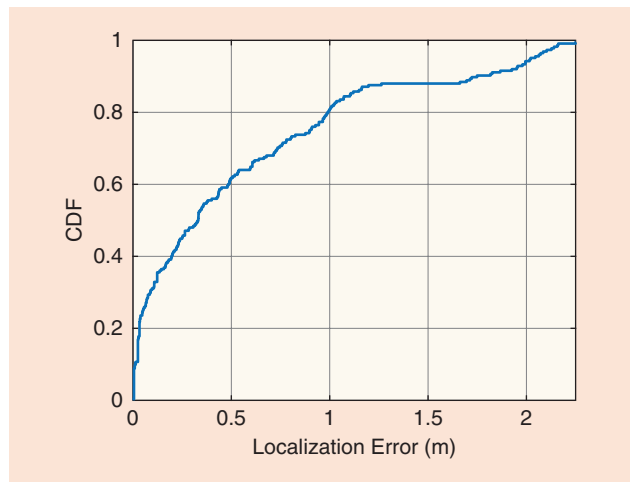


FIGURE 12. The empirical CDF of the position error.

where the maximal absolute value appearing in the numerator can compensate possible synchronization errors;  $N_{\text{tap}}$  denotes the length of the CIR vector, i.e., the number of taps;  $*$  denotes the convolution operator; and  $\mathbf{g}_{T,2}$  is the time-domain TR signature of  $\mathbf{h}_{T,2}$ , as  $g_{T,2}[k] = h_{T,2}^*[N_{\text{tap}} - k - 1]$ ,  $k = 0, 1, \dots, N_{\text{tap}} - 1$ .

During the online monitoring phase, the receiver keeps searching for the match between the current estimated CSI and the one in  $\mathcal{G}$  by locating the strongest TRRS. The TRRS between the unknown testing CSI  $\mathbf{H}_{T,\text{test}}$  and the trained event  $S_i$  is defined as

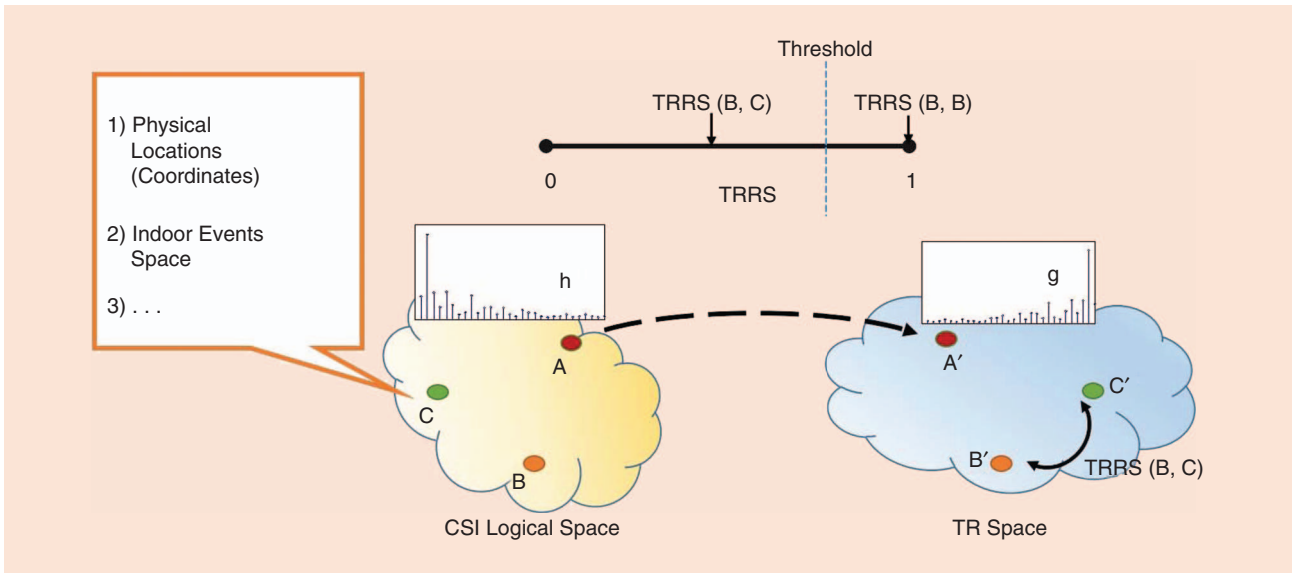


FIGURE 13. An illustration of mapping between the CSI logical space and the TR space.

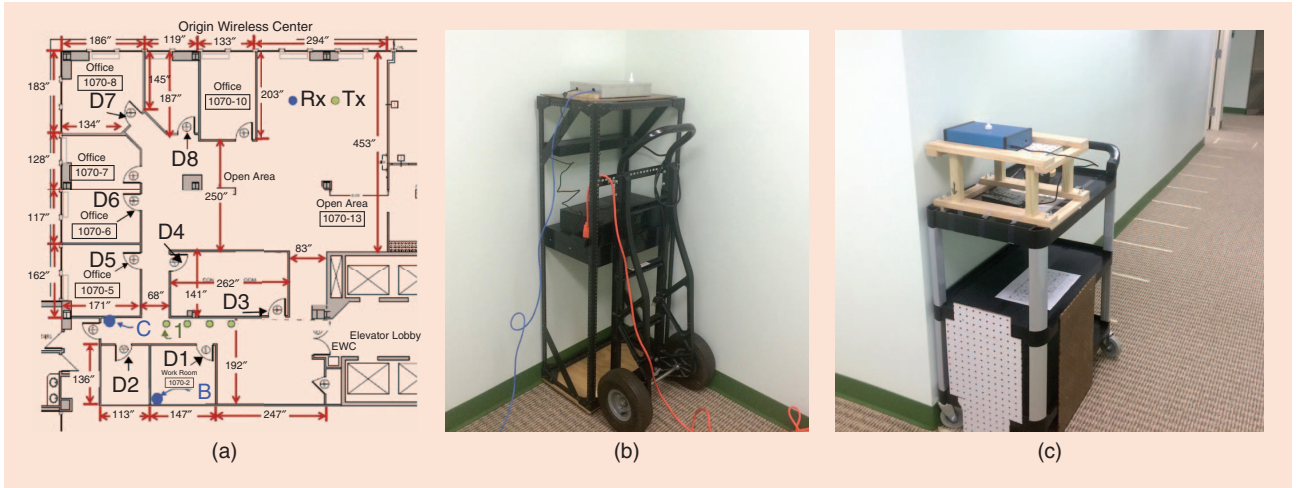


FIGURE 14. The experimental setting. (a) The floor plan, (b) the radio station: receiver, and (c) the radio station: transmitter [62].

$$\mathcal{TR}_S(\mathbf{H}_{T,\text{test}}) = \max_{\mathbf{h}_{T,\text{test}} \in \mathbf{H}_{T,\text{test}}} \max_{\mathbf{h}_{T,i} \in \mathbf{H}_{T,i}} \mathcal{TR}(\mathbf{h}_{T,\text{test}}, \mathbf{h}_{T,i}), \quad (12)$$

where  $\mathbf{H}_{T,\text{test}}$  denotes a group of testing CSI samples assumed to be drawn from the same state at  $M$  different time instances, i.e.,  $\mathbf{H}_{T,\text{test}} = [\mathbf{h}_{T,\text{test}}(t_0), \mathbf{h}_{T,\text{test}}(t_1), \dots, \mathbf{h}_{T,\text{test}}(t_{M-1})]$ .

Once we obtain the TRRS for each event, we can find the most likely state for the testing CSI matrix  $\tilde{\mathbf{H}}$  by searching for the maximum among  $\mathcal{TR}_S(\tilde{\mathbf{H}})$ ,  $\forall i$ , as

$$S^* = \begin{cases} \operatorname{argmax}_{S_i \in \mathcal{D}} \mathcal{TR}_S(\mathbf{H}_{T,\text{test}}), & \text{if } \max_{S_i \in \mathcal{D}} \mathcal{TR}_S(\mathbf{H}_{T,\text{test}}) \geq \Gamma \\ \text{unknown}, & \text{otherwise} \end{cases}, \quad (13)$$

where the superscript  $*$  on  $S$  denotes the optimal. To avoid false alarms introduced by events outside of the trained set  $\mathcal{D}$ , the TRIEDS adopts a threshold-trigger mechanism such that the occurrence of event  $S^*$  is reported if and only if the TRRS  $\mathcal{TR}_S(\mathbf{H}_{T,\text{test}})$  reaches a predefined threshold  $\Gamma$ .

## Experiments

We evaluated the TRIEDS's performance through experiments on detecting states of multiple door openings and closings in a typical office environment during weekday working hours. We also evaluated the received signal strength indicator (RSSI)-based indoor detecting approach [10], which differentiates different doors' open or closed state through RSSI change patterns, and we compared it with the TRIEDS.

During the experiment, as shown in Figure 14(a), we placed the radio frequency (RF) receiver on either location B or C, and we set the transmitter on one of the 1-m-separated points, designated *axis 1, 2, 3, and 4*, represented by the green dots in the figure. In total, then, there were two receiver locations and four transmitter locations, resulting in eight transmitter–receiver location possibilities. The TRIEDS's task was to detect which wooden door among doors D1–D8, as marked in Figure 14(a), was closed versus all of the other doors being

open. In Table 1, all of the trained indoor events are listed. For each transmitter–receiver location and each potential event, we measured 3,000 CSI samples.

When the receiver was on location B, the transmission between the transmitter and the receiver was NLOS because of the absence of a direct LOS link. On the other hand, when the receiver was on location C, no matter which green dot the transmitter was on, it was transmitting under LOS, which led to a dominant multipath component existing in the multipath CSI. An example of the multipath CSI with respect to the open and closed states of door D1 is shown in Figure 15(a) and (b), where the dominant path remains the same and contains most of the energy in the CSI, while other multipath components are distinct under the open and closed states. In Figure 15(c), we show the TRRS between different indoor events. As different colors represent different values of the TRRS, the TRIEDS is capable of distinguishing between different indoor events through the TRRS.

The overall false alarm and detection rate for the TRIEDS and the RSSI-based approach are listed in Tables 2 and 3. We find that the performance of the TRIEDS is superior to that of the RSSI-based approach, as it achieves a better detection rate and a lower false alarm rate. Even in an office environment with human activities, the TRIEDS can maintain a detection rate higher than 96.92% and a false alarm rate lower than 3.08% under NLOS, as well as a detection rate higher than 97.89% and a false alarm rate lower than 2.11% under LOS.

We can see from the experimental results that the TRIEDS captures the variations in the CSI, maps different multipath profiles of indoor events into separate points in the TR space, compresses the complex-valued features into a real-valued scalar TRRS, and supports the simplest detection and clas-

**Table 1. A state list for TRIEDS to detect.**

State Index	Description
$S_1$	All of the doors are open.
$S_{i+1}$	Door D1 is closed and the others are open. $\forall i = 1, 2, \dots, 8.$

sification algorithms, producing a good performance. When the surrounding environment is dynamic, changes introduced to the CSI can be harmful to the TRIEDS's performance, depending on how significantly the multipath profile changes. For example, if there was a furniture rearrangement introducing great changes to the majority of the multipaths, the space would need reprofiling, and the training database would require updating to maintain detection performance. However, if the environmental change affected only a few multipaths and the distinct feature in the CSI was preserved—e.g., when changes happened far away from the transmitter and the receiver or only a small object moved—system performance could be guaranteed without reprofiling the space. In [62], the researchers utilized the CSI to detect door states in a single-family house for two weeks with normal resident activities. As shown by these long-term experiments, the system can achieve an accuracy of over 90% without reprofiling all of the training events.

### Human radio biometrics

Automated recognition of persons based on their biological and behavioral characteristics involves well-known features, including fingerprints, face, irises, and voice [63], [64]. Since biometrics for individuals are inherent and unique, such traits have become widely used in surveillance and authentication systems for human identification. Because of the difficulty in

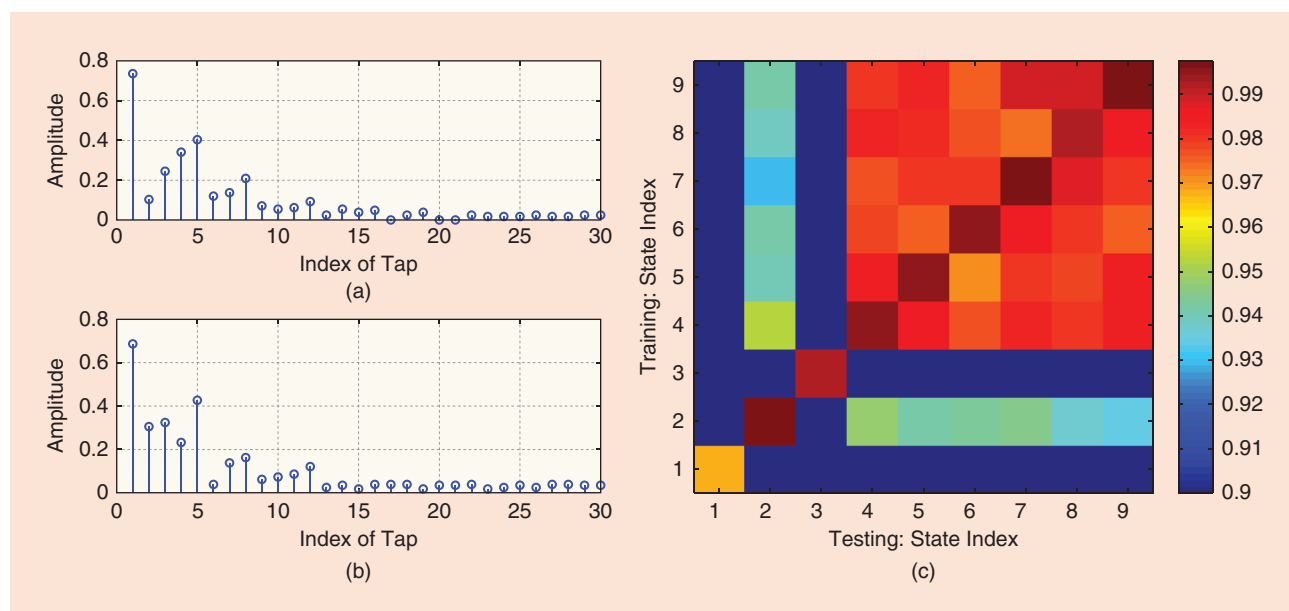


**FIGURE 15.** A feasibility demonstration. The multipath profiles (amplitude part) for different states of door D1 under location C with (a) door open and (b) door closed. (c) A resonance strength map with the receiver on location C and the transmitter on the first green dot (axis 1) [62].

**Table 2. The false alarm and detection probability for NLOS multievent detection by the TRIEDS in a normal environment (location B) [62].**

LOC B	Axis 1	Axis 2	Axis 3	Axis 4
TRIEDS detection rate (%)	96.92	98.95	99.23	99.4
TRIEDS false alarm rate (%)	3.08	1.05	0.77	0.6
RSSI detection rate (%)	92.5	94.16	94.77	95.36
RSSI false alarm rate (%)	7.5	5.84	5.23	4.64

**Table 3. The false alarm and detection probability for LOS multievent detection by the TRIEDS in a normal environment (location C) [62].**

LOC C	Axis 1	Axis 2	Axis 3	Axis 4
TRIEDS detection rate (%)	97.89	98.94	99.18	99.36
TRIEDS false alarm rate (%)	2.11	1.06	0.82	0.64
RSSI detection rate (%)	96.73	97.19	97.35	97.43
RSSI false alarm rate (%)	3.27	2.81	2.65	2.57

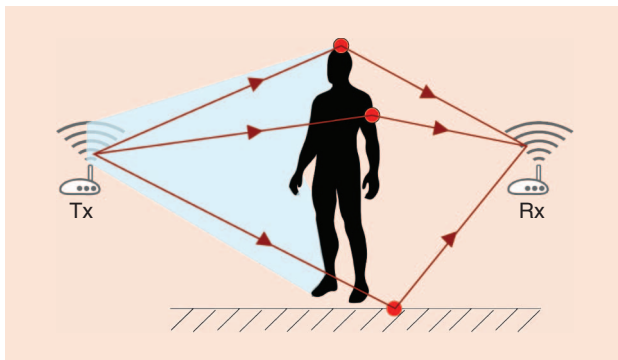


**FIGURE 16.** A demonstration of radio propagation around a human body [77].

counterfeiting biometrics, techniques based on biological individualities are good at countering growing security threats and facilitating personalization and convenience, possessing clear-cut advantages over traditional security methods, such as passwords and signatures.

Although current biometrics systems are accurate and can be applied in all environments, all of them require special devices that capture human biometric traits in an extremely LOS environment—i.e., the subject must make contact with the devices. In this section, we discuss a novel concept of radio biometrics utilizing the multipath CSI, based on which accurate human identification and verification can be implemented with commercial Wi-Fi devices, even in a through-the-wall setting.

### CSI as human biometrics

The relationship between human physical characteristics and the absorption of EM waves by human bodies has been studied in the carrier frequency range of 1–15 GHz, where Melia found that the body’s surface area has a dominant effect on absorption [65]. Other researchers further studied the interaction of EM waves with biological tissues [66] and measured

these tissues’ dielectric properties [67], [68]. According to the literature, the wireless propagation pattern around a human body depends highly on individual physical characteristics (e.g., height and mass), the total body water volume, the skin condition, and the characteristics of other biological tissues. The work in [76] first proposed the concept of human radio biometrics and defined it as the human-affected wireless signal under attenuations and alterations, containing individual identity information. The term *radio shot* is defined as the procedure of taking and recording human radio biometrics via RF signals (such as Wi-Fi).

Radio biometrics can be viewed as unique for each human being. Take the DNA sequence as an example. All humans are 99.5% similar in terms of DNA sequence, but no two are genetically identical, which is the key to techniques such as genetic fingerprinting [69]. Considering the combination of all of the physical characteristics and other biological features that affect the propagation of EM waves around the human body and how variable those features can be among different individuals, the chance for two humans to have identical combinations is significantly small, no matter how similar those features might be. Consequently, a person’s radio biometrics, which reflect how wireless signals interact with the human body, can be viewed as unique.

The human body acts as an RF reflector and absorber in an indoor wireless signal propagation environment. Radio propagation around the human body is demonstrated in Figure 16, where the red dots represent the reflecting and scattering points due to the human body and other objects. As seen from the figure, human radio biometrics are implicitly embedded in the multipath CSI profile. However, the human body may affect only a few paths of the multipath CSI, and the energy of those paths is small because of the low reflectivity and permittivity compared with other static objects, such as the walls and furniture. As a result, human radio biometrics captured through radio shot are buried in the CSI by other useless components.

Furthermore, because the raw CSI obtained from Wi-Fi chips is a large-scale, complex-valued matrix, the resulting raw radio biometrics are high dimensional and complex valued, which further complicates the identification problem and increases the computation complexity. To tackle the above problem, we discuss several postprocessing algorithms to calculate an analytic based on the TR technique that extracts the human radio biometrics and emphasizes the differences among individual radio biometrics.

### TR-based human identification

TR-based human identification exploits the human radio biometrics embedded in the CSI and consists of the following two key components:

- **Human radio biometrics refinement:** This module extracts the human biometric information from the raw CSI measurement, which is a complex-valued matrix. Because of the independence of each link, the background for each must be calculated and compensated for individually. An important consideration is that each CSI measurement may

be corrupted by the sampling frequency offset and the symbol timing offset. Hence, before background calculation and compensation, the phase of each CSI measurement must be aligned. After alignment, based on the assumption that the human radio biometrics contribute to only small changes in the multipath, the background can be obtained by taking the average of several CSI measurements.

- *TR-based identification:* Once the complex-valued human radio biometrics information is refined, this component simplifies the identification problem by reducing the high-dimensional, complex-valued feature to a real-valued scalar. By leveraging the TR technique, the human radio biometrics are mapped onto the TR space, and the TRRS quantifies the differences between different radio biometrics.

Mathematically, the frequency-domain CSI, i.e., the CFR, for the  $m$ th link with the presence of human  $i$  can be decoupled into a common CSI component and the human radio biometric component:

$$\mathbf{h}_{F,i}^{(m)} = \mathbf{h}_{F,0}^{(m)} + \delta\mathbf{h}_{F,i}^{(m)}, \quad i = 1, 2, \dots, N, \quad (14)$$

where  $\mathbf{h}_{F,i}^{(m)}$  is a  $N_{\text{sub}} \times 1$  complex-valued vector, which denotes the CSI when the  $i$ th individual is present.  $N$  is the number of individuals to be identified, and  $N_{\text{sub}}$  is the number of subcarriers, i.e., the length of the CSI. The static CSI component  $\mathbf{h}_{F,0}^{(m)}$  is generated from the static environment in the absence of a human, and  $\delta\mathbf{h}_{F,i}^{(m)}$  denotes the perturbation in the CSI caused by the  $i$ th individual. Here, the  $\delta\mathbf{h}_{F,i}^{(m)}$  is the raw human radio biometric information of the  $i$ th individual embedding in the CSI of the  $m$ th link.

### Radio biometrics refinement

In the CSI model in (14), the radio biometrics  $\delta\mathbf{h}_{F,i}^{(m)}$  also consist of two parts: the common radio biometric information and the distinct radio biometric information. Thus,  $\mathbf{h}_i^{(m)}$  can be further decomposed as

$$\mathbf{h}_{F,i}^{(m)} = \mathbf{h}_{F,0}^{(m)} + \delta\mathbf{h}_{F,i,c}^{(m)} + \delta\mathbf{h}_{F,i,d}^{(m)}, \quad \forall i, m, \quad (15)$$

where  $\delta\mathbf{h}_{F,i,c}^{(m)}$  represents the common radio biometric information determined by all of the  $N$  participants in the identification system and  $\delta\mathbf{h}_{F,i,d}^{(m)}$  is the individual distinct radio biometric information.

To extract the distinct radio biometrics  $\delta\mathbf{h}_{F,i,d}^{(m)}$ , we must first estimate the background information in the CSI  $\mathbf{h}_{F,0}^{(m)} + \delta\mathbf{h}_{F,i,c}^{(m)}$ . Then, we can extract the distinct human radio biometrics for each individual on link  $m$ , i.e., the  $\tilde{\mathbf{h}}_{F,i}^{(m)}$ , by subtracting a scaled version of the background component from the original CSI, as

$$\tilde{\mathbf{h}}_{F,i}^{(m)} = \mathbf{h}_{F,i}^{(m)} - \frac{\alpha}{N} \sum_{i=1}^N \frac{\mathbf{h}_{F,i}^{(m)}}{\|\mathbf{h}_{F,i}^{(m)}\|^2}, \quad (16)$$

where  $\frac{1}{N} \sum_{i=1}^N \mathbf{h}_{F,i}^{(m)} / \|\mathbf{h}_{F,i}^{(m)}\|^2$  is the estimation of the background information in the CSI and  $\alpha \in [0, 1]$  is the background subtraction factor. A typical value of  $\alpha$  is 0.5.

Because of the MIMO transmission, the radio biometrics of each individual is a matrix, i.e.,  $\mathbf{H}_{F,i} = [\tilde{\mathbf{h}}_{F,i}^{(1)}, \tilde{\mathbf{h}}_{F,i}^{(2)}, \dots, \tilde{\mathbf{h}}_{F,i}^{(N_{\text{link}})}]$ ,  $\forall i$ , where  $N_{\text{link}}$  is the number of transmitter–receiver links in the MIMO system.

### Identification methodology

After taking the radio shot by means of the TR signal processing, we map the high-dimensional, complex-valued human radio biometrics embedded in the CSI measurements into the TR space, and we reduce the feature dimension from  $L \times M$  to 1. We can implement the human recognition problem as a simple multiclass classification problem, where we measure the similarity between training and testing features by the value of the TRRS.

Let us denote the TRRS between two CFRs  $\mathbf{h}_{F,1}$  and  $\mathbf{h}_{F,2}$  as  $\mathcal{TR}(\mathbf{h}_{F,1}, \mathbf{h}_{F,2})$ . Then, the TRRS between two radio biometric matrices  $\mathbf{H}_{F,i}$  and  $\mathbf{H}_{F,j}$  is defined as the average of the TRRSs on each of the links, i.e.,

$$\mathcal{TR}(\mathbf{H}_{F,i}, \mathbf{H}_{F,j}) = \frac{1}{M} \sum_{m=1}^M \mathcal{TR}(\tilde{\mathbf{h}}_{F,i}^{(m)}, \tilde{\mathbf{h}}_{F,j}^{(m)}). \quad (17)$$

For any radio biometric measurement  $\mathbf{H}_{F,\text{test}}$ , given a training database consisting of the radio biometrics of each individual  $\mathbf{H}_{F,i} \forall i$ , the predicted individual identity is determined based on the TRRS, as shown in (18), where  $\Gamma$  is a predefined threshold for triggering the identification, and  $\hat{i} = 0$  denotes an unidentified individual.

$$\hat{i} = \begin{cases} \operatorname{argmax}_i \mathcal{TR}(\mathbf{H}_{F,\text{test}}, \mathbf{H}_{F,i}), & \text{if } \max_i \mathcal{TR}(\mathbf{H}_{F,\text{test}}, \mathbf{H}_{F,i}) \geq \Gamma, \\ 0, & \text{otherwise.} \end{cases} \quad (18)$$

### Experiments

We conducted experiments to evaluate both the accuracy of the TR-based human identification system and the impact introduced by the inconsistency in human poses. The test setting is depicted in Figure 17(a), where a tester stands on the footprint in a closed room between the transmitter and the receiver, which are marked as circles.

To analyze the feasibility and accuracy of identifying individuals using human radio biometrics, we tested the system to differentiate among 11 individuals, and the corresponding ROC curve is plotted in Figure 17(b). With a threshold  $\Gamma$  being 0.91, the average identification rate was 98.78%, while the false alarm rate was 9.75%. A false alarm was introduced mainly when two individuals had similar body contours, such that the possibility of misclassification between them increased. However, since the permittivity and conductivity of body tissues, which are more distinct between different individuals, also affected the Wi-Fi signal propagation that encountered the human body, the identification accuracy was still high.

In the next experiment, we studied the impact of the inconsistency in human poses between the training and testing phases on the identification accuracy. We asked four participants to stand at the same location and assume five different poses by lifting their arm at various angles and in different directions,

as shown in Figure 17(c). The corresponding ROC curves are shown in Figure 17(d). When the testing samples came from the same pose, the identification rate reached 97.67%, with a false alarm rate of 5.58%. However, as the participants progressively changed their poses from the second pose to the fifth, the identification rate dropped from 95.66% to 88.06%, 58.83%, and 79.29%, respectively, with a false alarm rate around 5.6%. The system was robust to slight changes in posture, e.g., from pose 1 to pose 2. However, as shown by the ROC curve of testing over pose 4, when the pose considerably alters the propagation environment, the TR-based human identification system may have difficulty finding a match in the training database.

Hence, when the poses or the standing locations change, the multipath profiles in the TR space might fall out of the person's proximity (the range of high similarity), which degrades the identification rate.

### Wireless vital signs monitoring

Since the CSI can capture environmental perturbations due to human activities, the features of different behaviors can be extracted by analyzing the CSI. Among the various human activities, breathing is an important one, since it is a fundamental physiological function that can act as a vital indicator and predictor of health status. Although breathing introduces very

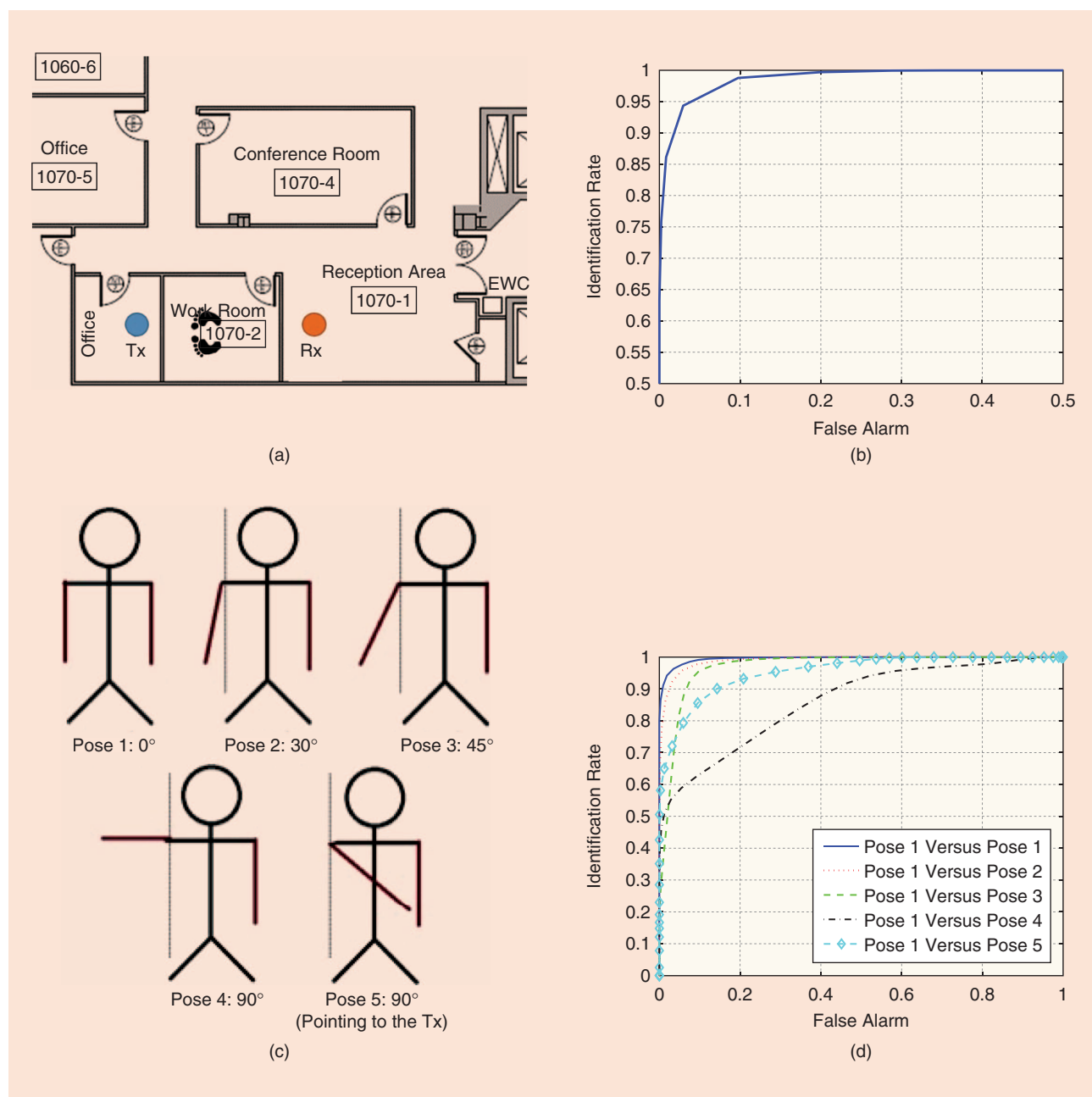


**FIGURE 17.** The experiments on human radio biometrics. (a) The test setting floor plan; (b) the ROC curve of identifying 11 individuals; (c) a demonstration of different poses; and (d) the ROC curve of identifying four individuals with different training and testing poses [77].

minor environmental perturbations and affects CSIs only slightly, the periodic pattern of breathing embedded in the CSI time series is very distinct and can be extracted with high fidelity.

### CSI model in the presence of breathing

To better understand the impact of breathing on CSI values, let us start with a time-varying CSI (CFR) model without environmental perturbations as

$$h_F^{(k)}(t) = \sum_{\ell=1}^L \zeta_{\ell} e^{-j2\pi \frac{d_{\ell}}{\lambda_k}} + e^{(k)}(t), \quad (19)$$

where  $k \in \mathcal{V}$  and  $\mathcal{V}$  denotes the set of usable subcarriers with a total of  $N_{\text{sub}}$  usable subcarriers,  $L$  is the total number of multipaths,  $\zeta_{\ell}$  is the complex gain of multipath  $\ell$ ,  $d_{\ell}$  is the length of multipath  $\ell$ , and  $\lambda_k$  is the wavelength of subcarrier  $k$  given by  $\lambda_k = c/(f_c(k/N_{\text{DFT}}T_s))$ . Here,  $f_c$  is the carrier frequency,  $c$  is the speed of light,  $T_s$  is the sampling interval given as  $T_s = 1/B$  where  $B$  is the baseband bandwidth of the Wi-Fi signals, and  $N_{\text{DFT}}$  is the size of the discrete Fourier transform. The function  $e^{(k)}(t)$  is the thermal noise on subcarrier  $k$  at time  $t$ . Without environmental perturbations, the multipath gains and delays are time invariant.

With breathing, one or more multipath gains and delays become time varying and introduce periodic variations into the CSI values. Figure 18 demonstrates an example of how breathing affects CSI values received on Wi-Fi devices. For

simplicity, we assume that breathing affects only multipath 1 and the gain of multipath 1 takes the form of [44]

$$\zeta_1(t) = \zeta_1 \times \left( 1 + \frac{\Delta d_1}{d_1} \sin \theta \sin \left( \frac{2\pi b}{60} t + \phi \right) \right)^{-\psi}, \quad (20)$$

where  $\zeta_1$  and  $d_1$  are the gain and path length for multipath 1 in a static environment,  $\Delta d_1$  is the additional positional displacement of multipath 1 caused by breathing,  $\psi$  is the path-loss exponent,  $\theta$  is the angle between the subject and the impinging EM wave,  $b$  is the breathing rate measured in breaths per minute, and  $\phi$  is the initial breathing phase. Given that  $d_1 \gg \Delta d_1$ ,  $\zeta_1(t)$  can be approximated by the time-invariant multipath gain  $\zeta_1$ .

Meanwhile, breathing affects the phase of multipath 1 by changing its path length  $d_1(t)$ , expressed as

$$d_1(t) = d_1 + \Delta d_1 \sin \theta \sin \left( \frac{2\pi b}{60} t + \phi \right). \quad (21)$$

Substituting (19) and (21) into (18), we have

$$h_F^{(k)}(t) = \zeta_1 e^{-j2\pi \frac{d_1}{\lambda_k}} e^{-j2\pi \frac{\Delta d_1 \sin \theta \sin \left( \frac{2\pi b}{60} t + \phi \right)}{\lambda_k}} + \sum_{\ell=2}^L \zeta_{\ell} e^{-j2\pi \frac{d_{\ell}}{\lambda_k}} + e^{(k)}(t). \quad (22)$$

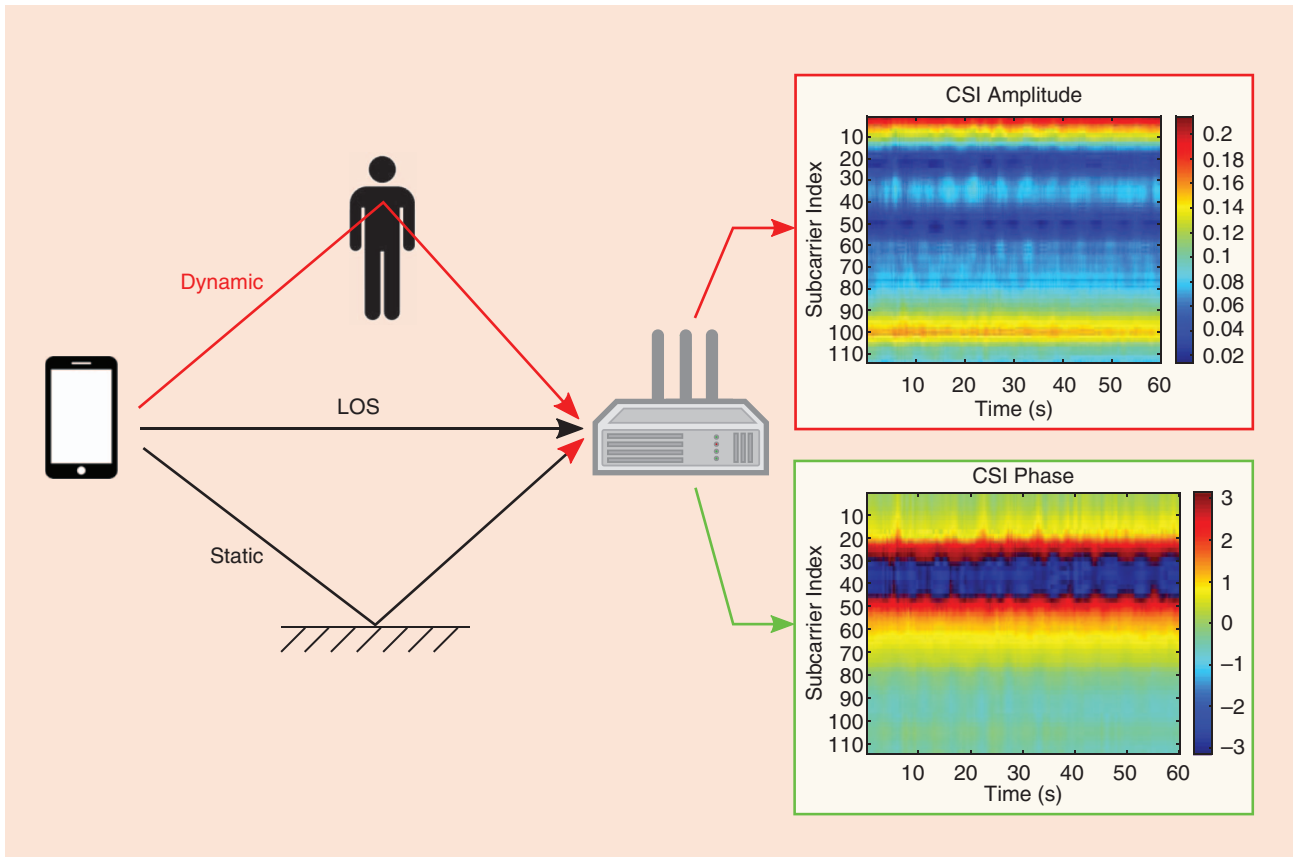


FIGURE 18. The impact of breathing on CSIs.

The first term on the right-hand side of  $H_k(t)$  in (22) can be decomposed into an infinite summation according to the Jacobi–Anger expansion [45], given as

$$e^{-j2\pi \frac{\Delta d_1 \sin \theta \sin(\frac{2\pi b}{60}t + \phi)}{\lambda_k}} = \sum_{m=-\infty}^{+\infty} (-1)^m J_m(\nu_k) e^{jm \frac{2\pi b}{60}t} e^{jm\phi}, \quad (23)$$

where  $\nu_k = 2\pi \sin \theta \Delta d_1 / \lambda_k$  and  $J_m(x)$  is the  $m$ th-order Bessel function with argument  $x$ .

In practice,  $J_m(\nu_k)$  decays rapidly for  $|m| \geq 2$ , given typical values of  $\nu_k$ , and  $H_k(t)$  can be approximated as

$$h_F^{(k)}(t) \approx \underbrace{\zeta_1 e^{-j2\pi \frac{d_1}{\lambda_k} t} \sum_{m=-1}^{+1} (-1)^m J_m(\nu_k) e^{jm \frac{2\pi b}{60}t} e^{jm\phi}}_{S^{(k)}(t)} + \underbrace{\sum_{\ell=2}^L \zeta_\ell e^{-j2\pi \frac{d_\ell}{\lambda_k} t}}_{I^{(k)}} + e^{(k)}(t), \quad (24)$$

where  $S^{(k)}(t)$  stands for the useful signal for breathing monitoring on subcarrier  $k$  and  $I^{(k)}$  represents the time-invariant part due to the static environment and is regarded as the interference. Notice that the dynamic model of  $h_F^{(k)}(t)$  shown in (24) can be easily extended to multiperson cases.

### Breathing monitoring using CSI values

As breathing introduces periodic variations into the CSI time series, to extract the breathing rate, we can calculate the pairwise complex-valued TRRS between any two CSI values in the time series, which encapsulates variations of both CSI amplitudes and phases, given as

$$\mathcal{TR}(h_{F,i}, h_{F,m}) = \frac{\sum_{k=1}^{N_{\text{sub}}} h_{F,i}[k] h_{F,m}^*[k] e^{-j(\omega^* + \kappa^* k)}}{\|h_{F,i}\|_2 \|h_{F,j}\|_2}, \quad i, m = 1, 2, \dots, N, \quad (25)$$

where  $N$  is the number of CSI vectors and  $\mathbf{h}_{F,i} = \{h_{F,i}^{(k)}\}_{k \in \mathcal{V}} = [h_{F,i}[1], \dots, h_{F,i}[N_{\text{sub}}]]$  is the CSI vector composed by all

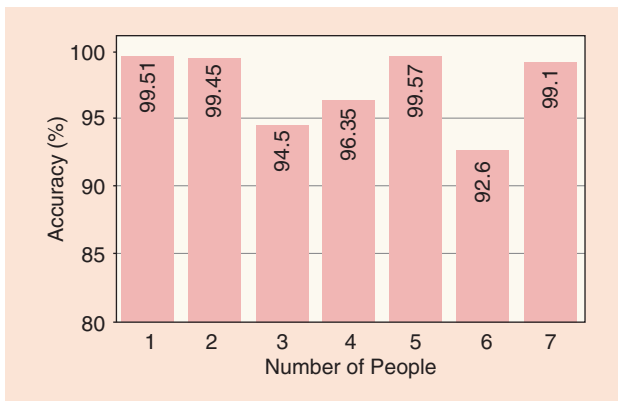


FIGURE 19. The accuracy with multiple people under the NLOS scenario.

of the subcarriers received at the  $i$ th time instance. We introduce  $\omega^*$  and  $\kappa^*$  in (25) to remove the initial and linear phase distortions.

The TRRS matrix  $\mathbf{R}$  includes all of the pairwise TRRS values. Assuming a total of  $N$  CSI vectors, the  $(i, m)$ th entry of the  $N \times N$  TRRS matrix  $\mathbf{R}$  is given by  $\mathbf{R}_{i,m}$ , as shown in (25).

After this, the breathing rates can be extracted from the TRRS matrix via a spectral analyzer, e.g., based on the Root-MUSIC algorithm [46]. If we denote the  $2N - 2$  complex roots by  $\hat{\mathbf{z}} = \{\hat{z}_1, \hat{z}_2, \hat{z}_3, \dots, \hat{z}_{2N-2}\}$ , then one can choose  $p$  out of the  $N - 1$  complex roots closest to the unit circle, where  $p$  is the signal subspace dimension. The breathing rate estimation can be formulated as  $\hat{b}_i = 60 \times (\angle \hat{z}_i / 2\pi T_s)$ ,  $i = 1, 2, \dots, p$ , where  $T_s$  is the sampling interval and  $\angle(x)$  is the operator that extracts the phase from the complex argument  $x$ .

In reality, breathing rates are limited to a finite range  $[b_{\min}, b_{\max}]$ , since a person cannot breathe extremely quickly or slowly. Thus, we sift the breathing rate estimations  $\hat{\mathbf{b}} = [\hat{b}_1, \hat{b}_2, \dots, \hat{b}_p]$  by discarding those outside the range of  $[b_{\min}, b_{\max}]$ , which leads to  $\hat{\mathbf{b}} = [\hat{b}_{r_1}, \hat{b}_{r_2}, \dots, \hat{b}_{r_{p'}}]$ , where  $p'$  is the number of the remaining complex roots and  $r_i$  is the index of the  $i$ th remaining estimation.

For CSIs measured on  $N_{\text{ch1}}$  Wi-Fi channels and with  $N_{\text{link}}$  antenna links, the set  $\hat{\mathbf{b}}$  can be written as the union of the estimated breathing rates calculated on all Wi-Fi channels and antenna links, i.e.,  $\hat{\mathbf{b}} = \bigcup_{s=1}^{N_{\text{link}}} \bigcup_{f=1}^{N_{\text{ch1}}} \hat{\mathbf{b}}^{(s,f)}$ , where  $\hat{\mathbf{b}}^{(s,f)}$  is the breathing rate estimation obtained on the  $s$ th antenna link and  $f$ th Wi-Fi channel.

We can also extend the breathing rate estimation to a multiperson breathing monitoring case by running a clustering algorithm, e.g., affinity propagation [47], on the estimated breathing rates [81].

### Experimental results

We evaluated the performance of the breathing monitoring system by comparing the breathing rate estimations against the ground truths. To obtain the ground truths, each participant synchronized his or her breathing with a metronome.

Up to seven people were invited into a conference room, with two devices placed under NLOS for breathing monitoring. Figure 19 summarizes the performance accuracy, which shows that an accuracy of 99.1%, when  $K = 7$ , and a mean accuracy of 97.3% averaging over all seven cases were achieved.

### Related works and comparisons

As discussed in the previous sections, if one can create a large effective bandwidth with the aid of either antenna or frequency diversity, there will be large enough multipaths available to enable many cutting-edge IoT applications that are independent of the carrier frequency. Our experimental results showed that the CSI obtained using Wi-Fi chips with antenna diversity can render meaningful radio analytics. With more bandwidth possibly available in fifth generation, and thus more multipaths observed, one can expect even better performance. In addition, it is possible to implement these IoT applications with even just one antenna.

There are other radio analytics approaches in the literature. One is to leverage the radar concept to utilize the time of flight (ToF) for locationing [60], [71] and breathing monitoring [78]. There are a few drawbacks to obtaining the ToF, including the need to perfectly synchronize the devices and scan through a large spectrum, often with a range of several hundred megahertz or more. Thus, the hardware cost can be higher than with simply using commodity Wi-Fi or LTE devices. Furthermore, when in different environments, especially under NLOS conditions with different construction materials, some calibration or training must first be performed.

The presented TR techniques, however, do not require an LOS path between the transmitter and the receiver and can work as well in NLOS conditions. This leads to more flexibility in deploying the devices; e.g., only a few devices can cover a large area for positioning and tracking.

Another common practice to obtain the multipath CSI values is by means of ultrawide-band signal transmission [1], [14], which offers an ultralarge bandwidth to obtain a large number of multipaths. But because of regulations, the very low transmission power requirement may significantly limit the coverage and increase the infrastructure cost. As such, this solution is often used for close-range, LOS applications.

In the following, we will discuss in detail the existing approaches on indoor positioning and tracking, event detection, human radio biometrics, and breathing monitoring using RF signals.

### *Indoor positioning and tracking*

Although GPS has been widely deployed as a successful solution to outdoor positioning, many questions still remain concerning indoor positioning [1], [2], because the interior structure of a building is much more complex than the outdoor environment. Various indoor positioning techniques have been proposed, which can be mainly classified into four categories, based on vision, acoustic signals, IMU, and radio. The vision-based approaches, such as camera, laser, and so forth, suffer from high deployment and hardware costs, the need for sophisticated calibrations, and limited coverage, although a very high accuracy may be achieved. The acoustic-based techniques have only a limited range and are not scalable to a large number of users. The positioning accuracy of IMU-based methods is limited mainly by gyroscope drift and poor moving-distance estimation.

Because of the ubiquitousness and low cost of RF devices, radio-based IPSs, especially those founded on Wi-Fi, have become popular nowadays. Based on the principles they use, the radio-oriented indoor positioning schemes can be further categorized into two classes [1]: triangulation based and fingerprinting based. The features they utilize can be obtained either from the medium access control layer information, e.g., RSSI readings and the time stamps of the received packets at the receiver, or from the physical layer information, e.g., the CSI.

### *Triangulation based*

In the triangulation-based schemes, either the distance [19]–[21] or the angle [22]–[24] between a device and several anchors is estimated, and the position of the device can be inferred by performing geometrical triangulation. The distance between the device and anchor can be estimated from the RSSI decay [17] or from the ToF of the transmitted packets that can be extracted from the time stamps of the received packets [25]. The angle between the devices can be obtained by examining the features of the CSI values received by multiple receiver antennas, and then the angle of arrival of the direct path to the target can be found. However, the main challenges for the triangulation-based approaches are the blockage and reflection of the transmitted signal, since only the signal coming from the direct path between the device and anchor can be used for positioning.

### *Fingerprinting based*

In the fingerprinting-based schemes, the features can be obtained either from the vector of the RSSIs [17], [26] or the detailed CSI values [27], [28], [30] from a specific location to all of the anchors in range. A major drawback of the fingerprinting-based approach is that the features of the mapped locations are susceptible to environmental dynamics and the database of the mapped fingerprints needs to be updated before it can be used again. In addition, the computational complexity of fingerprinting-based approaches is high, and thus they are not feasible for low-latency applications.

Compared with these fingerprinting schemes, the centimeter-accuracy IPS discussed in this article fully exploits the spatial and frequency diversity of the multipath CSI to increase the effective bandwidth and enhance the robustness against environmental perturbations. The complexity of the feature calculation based on TRRS is also lower than most existing approaches. With the centimeter-accuracy IPS, many applications that need precise positioning can be enabled. For example, one may be able to design industry production lines that can accurately locate different parts, align them, and assemble them with much less human intervention. The mapping-free indoor tracking system can further reduce the implementation complexity, since it requires no feature matching as in the fingerprinting-based schemes and no recalibration. Most important, both of the two approaches can perform equally well under LOS and NLOS.

### *Indoor event detection*

Common features of RF signals to identify variations during signal transmission for indoor event detection include the RSSI and CSI. Because of its susceptibility to environmental changes, the RSSI has been applied to indicate and further recognize indoor activities [9], [10], [51], [52]. However, because the RSSI is coarse-grained and can be easily corrupted by the multipath effect, RSS-based sensing systems often require an LOS transmission, resulting in limited accuracy in indoor activity detection. Furthermore, CSI, including the amplitude and the phase, is now accessible in many commercial

devices and has been used for indoor event detection [11], [53]–[58]. However, most aforementioned CSI-based indoor sensing systems rely on only the CSI amplitudes, whereas the phase information is discarded regardless of how informative it may be.

Another technology category of device-free indoor monitoring systems is adopted from radar imaging technology to track targets [59], [60], [70], [71]. However, their techniques consume over 1 GHz of bandwidth and require a specially designed RF signal to sense the environment. Recently, Ohara et al. introduced a new method for indoor event detection by recognizing and classifying CSI with a deep neural network (DNN) composed of three convolutional layers and two recurrent layers [72]. However, because of the nature of DNNs, the complexity of training data collection and network learning is extremely high. In contrast, by leveraging the TR technique to exploit rich CSI, the proposed TRIEDS introduces a novel and practical solution that can well support through-the-wall detection and requires only low-complexity, single-antenna hardware operating in the ISM band.

### *Human radio biometrics*

Traditional biometrics systems, including fingerprint, face, and iris recognition, are accurate. However, they require special devices to capture human biometric traits in an extremely LOS environment, i.e., the subject must make contact with the devices. Another category of biometrics is gait analysis. It relies on the individual walking pattern to distinguish identity. Conventional gait recognition requires high-speed cameras, wearable sensors, and floor sensors [73].

Recently, gait recognition has been extended to an RF platform where the Doppler shift or the ToF of the signal reflected by the human body is used to extract the individual gait pattern [70], [74], [75]. However, to get a high-resolution gait profile, it relies on special devices to scan over an ultrawide spectrum, and LOS transmission is often required to guarantee the accuracy of the extraction. Moreover, the computational complexity introduced by the necessary image processing and machine learning algorithms for gait recognition is high. Unlike the aforementioned system, the proposed human identification system is based on radio biometrics and is thus capable of distinguishing and identifying different individuals through walls accurately with commercial Wi-Fi devices. In addition, the proposed system can support simple and efficient algorithms to achieve high-accuracy performance.

### *Breathing monitoring*

Contact-free breathing monitoring schemes have been developed to overcome the drawbacks of conventional breathing monitoring methods requiring physical contact with human bodies. Among them, schemes using EM waves are favorable, since they can monitor breathing rates through the wall in a highly complicated indoor environment. In terms of techniques, they can be classified into radar based and Wi-Fi based.

Among the radar-based schemes, Doppler radar is commonly used, which measures the frequency shift of the signals caused by the periodic variations of the EM waves reflected from human bodies [77]. Recently, Adib et al. presented a vital signs monitoring system that uses the Universal Software Radio Peripheral as the RF front end to emulate a frequency modulated continuous radar [78]. However, the requirement of specialized hardware introduces a significant deployment cost. In addition, the regulation on the transmission power significantly limits the range the system can monitor.

For the Wi-Fi-based schemes, RSSI is often used because of its availability on many Wi-Fi devices. In [79], Abdelnasser et al. presented UbiBreathe, which harnesses RSSI on Wi-Fi devices for breathing estimation. However, UbiBreathe is accurate only when users hold the Wi-Fi device close to their chest. More recently, CSIs were used for breathing monitoring. The scheme proposed by Liu et al. in [80] is one of the first few CSI-based breathing monitoring approaches. Nevertheless, a periodogram is used for spectral analysis, which needs a relatively long time for accurate breathing monitoring.

Compared with the aforementioned methods, the proposed breathing monitoring scheme is infrastructure free, since it utilizes off-the-shelf Wi-Fi devices. Furthermore, with the Root-MUSIC algorithm, the proposed approach can achieve highly accurate breathing rate estimations within a short period of time, and it can resolve the breathing rates of multiple people concurrently.

## **Conclusions**

As a revolutionary platform that connects everything around the world, the IoT has dramatically changed our lifestyle and enabled us to measure and track everything connected to it. Because of the ubiquitous deployment of wireless devices, wireless sensing that can make many smart IoT applications possible has recently received a great deal of attention. As the next generation of wireless systems embraces a larger bandwidth, richer information can be revealed through wireless sensing, e.g., in the form of multipaths. As bandwidth increases, the number of multipaths that can be resolved also increases, allowing them to serve as hundreds of virtual antennas.

Motivated by the physical principle of TR, we developed various radio analytics for smart IoT applications in indoor positioning, event detection, human recognition, and vital signs monitoring. Unlike conventional approaches for these applications, the proposed radio analytics approach can work well under NLOS and enjoys low implementation complexity, thus making it an ideal paradigm for smart IoT sensing, positioning, and tracking.

## **Authors**

**Beibei Wang** (bebewang@umd.edu) received her B.S. (highest honors) degree in electrical engineering from the University of Science and Technology of China, Hefei, in 2004 and her Ph.D. degree in electrical engineering from the University of Maryland, College Park, in 2009. She was a research associate

with the University of Maryland, College Park, from 2009 to 2010 and with Qualcomm Research and Development, San Diego, California, from 2010 to 2014. Since 2015, she has been with Origin Wireless Inc., Greenbelt, Maryland, as a chief scientist. Her current research interests include wireless communications and signal processing.

**Qinyi Xu** (qinyixu@umd.edu) received her B.S. (highest honors) degree in information engineering from Southeast University, Nanjing, China, in 2013. She is currently pursuing her Ph.D. degree in the Department of Electrical and Computer Engineering, University of Maryland, College Park. Her current research interests include signal processing and wireless communications.

**Chen Chen** (cc8834@umd.edu) received his B.S. and M.S. degrees from the Department of Microelectronics, Fudan University, Shanghai, China, in 2010 and 2013, respectively, and his Ph.D. degree from the Department of Electrical and Computer Engineering, University of Maryland, College Park, in 2017. He is currently a research scientist with Origin Wireless Inc., Greenbelt, Maryland. His research interests include biomedical signal processing and indoor localization.

**Feng Zhang** (fzhang15@umd.edu) received his B.S. and M.S. degrees from the Department of Electronic Engineering and Information Science, University of Science and Technology of China, Hefei, in 2011 and 2014, respectively. He is currently pursuing his Ph.D. degree in the Department of Electrical and Computer Engineering, University of Maryland, College Park. His research interests include time reversal communications, wireless sensing, and indoor localization.

**K.J. Ray Liu** (krljliu@umd.edu) was named a Distinguished Scholar-Teacher of the University of Maryland, College Park, in 2007, where he is the Christine Kim Eminent Professor of Information Technology. He was a recipient of the 2016 IEEE Leon K. Kirchmayer Award, IEEE Signal Processing Society 2014 Society Award, and 2009 Technical Achievement Award. He has won over a dozen best paper and invention awards. Recognized by Web of Science as a highly cited researcher, he is a fellow of the AAAS. He is the IEEE vice president-elect for technical activities and has been president of the IEEE Signal Processing Society and editor-in-chief of *IEEE Signal Processing Magazine*. He is a Fellow of the IEEE.

## References

[1] H. Liu, H. Darabi, P. Banerjee, and J. Liu, "Survey of wireless indoor positioning techniques and systems," *IEEE Trans. Syst., Man, Cybern. C*, vol. 37, no. 6, pp. 1067–1080, Nov. 2007.

[2] L. Dimitrios, J. Liu, X. Yang, R. R. Choudhury, V. Handziski, and S. Sen, "A realistic evaluation and comparison of indoor location technologies: Experiences and lessons learned," in *Proc. 14th ACM Int. Conf. Information Processing Sensor Networks*, 2015, pp. 178–189.

[3] M. Youssef, A. Youssef, C. Rieger, U. Shankar, and A. Agrawala, "Pinpoint: An asynchronous time-based location determination system," in *Proc. 4th ACM Int. Conf. Mobile Systems, Applications, and Services*, New York, 2006, pp. 165–176.

[4] R. J. Fontana and S. J. Gunderson, "Ultra-wideband precision asset location system," in *Proc. IEEE Conf. Ultra Wideband Systems and Technologies*, May 2002, pp. 147–150.

[5] D. Niculescu and B. Nath, "VOR base stations for indoor 802.11 positioning," in *Proc. 10th ACM Annu. Int. Conf. Mobile Computing and Networking*, New York, 2004, pp. 58–69.

[6] J. Xiong and K. Jamieson, "Arraytrack: A fine-grained indoor location system," in *Proc. 10th USENIX Symp. Networked Systems Design and Implementation*, 2013, pp. 71–84.

[7] Y. Zhao, "Standardization of mobile phone positioning for 3G systems," *IEEE Commun. Mag.*, vol. 40, no. 7, pp. 108–116, July 2002.

[8] G. Sun, J. Chen, W. Guo, and K. J. R. Liu, "Signal processing techniques in network-aided positioning: A survey of state-of-the-art positioning designs," *IEEE Signal Process. Mag.*, vol. 22, no. 4, pp. 12–23, July 2005.

[9] S. Sen, R. R. Choudhury, and N. Srihari, "Spin Once to Know Your Location," in *Proc. 12th ACM Workshop Mobile Computing Systems and Applications*, New York, 2012, pp. 1–6.

[10] S. Sigg, S. Shi, F. Buesching, Y. Ji, and L. Wolf, "Leveraging RF-channel fluctuation for activity recognition: Active and passive systems, continuous and RSSI-based signal features," in *Proc. ACM Int. Conf. Advances Mobile Computing and Multimedia*, 2013, pp. 43–52.

[11] K. Wu, J. Xiao, Y. Yi, D. Chen, X. Luo, and L. M. Ni, "CSI-based indoor localization," *IEEE Trans. Parallel Distrib. Syst.*, vol. 24, no. 7, pp. 1300–1309, July 2013.

[12] J. Hightower, R. Want, and G. Borriello, "SpotON: An indoor 3D location sensing technology based on RF signal strength," Dept. Computer Sci. Eng., Univ. Washington, Seattle, WA, Tech. Rep. UW CSE 00-02-02, Feb. 2000.

[13] X. Li, K. Pahlavan, M. Latva-aho, and M. Ylianttila, "Comparison of indoor geolocation methods in DSSS and OFDM wireless LAN systems," in *Proc. 52nd IEEE-VTS Fall Vehicular Technology Conf.*, 2000, vol. 6, pp. 3015–3020.

[14] N. Correal, S. Kyperountas, Q. Shi, and M. Welborn, "An UWB relative location system," in *Proc. IEEE Conf. Ultra Wideband Systems and Technologies*, Nov. 2003, pp. 394–397.

[15] P. Stegless and S. Gschwind, "The ubiquitous smart space platform" in *Proc. 3rd Int. Conf. Pervasive Computing*, 2005, pp. 73–76.

[16] B. Campbell, P. Dutta, B. Kempke, Y.-S. Kuo, and P. Pannuto, "Decawave: Exploring state of the art commercial localization," *Ann Arbor*, vol. 1001, no. 4, pp. 48109, 2015.

[17] M. Youssef and A. Agrawala, "The Horus WLAN location determination system," in *Proc. 3rd ACM Int. Conf. Mobile Systems, Applications, and Services*, New York, 2005, pp. 205–218.

[18] S. Sen, B. Radunovic, R. R. Choudhury, and T. Minka, "You are facing the Mona Lisa: Spot localization using PHY layer information," in *Proc. 10th ACM Int. Conf. Mobile Systems, Applications, and Services*, New York, 2012, pp. 183–196.

[19] D. Giustiniano and S. Mangold, "Caesar: carrier sense-based ranging in off-the-shelf 802.11 wireless LAN," in *Proc. 7th ACM Conf. Emerging Networking Experiments and Technologies*, 2011, pp. 10–21.

[20] S. Sen, D. Kim, S. Laroche, K.-H. Kim, and J. Lee, "Bringing CUPID indoor positioning system to practice," in *Proc. 24th Int. Conf. World Wide Web*, 2015, pp. 938–948.

[21] P. Bahl and V. N. Padmanabhan, "Radar: An in-building RF-based user location and tracking system," in *Proc. IEEE 19th Annu. Joint Conf. IEEE Computer and Communications Societies*, 2000, vol. 2, pp. 775–784.

[22] M. Kotaru, K. Joshi, D. Bharadia, and S. Katti, "SpotFi: Decimeter level localization using WiFi," in *Proc. 2015 ACM Conf. Special Interest Group on Data Communication*, pp. 269–282.

[23] J. Gjengset, J. Xiong, G. McPhillips, and K. Jamieson, "Phaser: Enabling phased array signal processing on commodity WiFi access points," in *Proc. 20th ACM Annu. Int. Conf. Mobile Computing and Networking*, 2014, pp. 153–164.

[24] S. Sen, J. Lee, K.-H. Kim, and P. Congdon, "Avoiding multipath to revive inbuilding WiFi localization," in *Proc. 11th ACM Annu. Int. Conf. Mobile Systems, Applications, and Services*, 2013, pp. 249–262.

[25] J. Xiong, K. Sundaresan, and K. Jamieson, "Tonetrack: Leveraging frequency-agile radios for time-based indoor wireless localization," in *Proc. 21st ACM Annu. Int. Conf. Mobile Computing and Networking*, 2015, pp. 537–549.

[26] P. Castro, P. Chiu, T. Kremenek, and R. Muntz, "A probabilistic room location service for wireless networked environments," in *Proc. Ubicomp 2001: Ubiquitous Computing*, Springer, 2001, pp. 18–34.

[27] X. Wang, L. Gao, S. Mao, and S. Pandey, "Deepfi: Deep learning for indoor fingerprinting using channel state information," in *Proc. IEEE Wireless Communications and Networking Conf.*, 2015, pp. 1666–1671.

[28] X. Wang, L. Gao, and S. Mao, "Phasefi: Phase fingerprinting for indoor localization with a deep learning approach," in *Proc. IEEE Global Communications Conf.*, 2015, pp. 1–6.

[29] S. Sen, B. Radunovic, R. Roy Choudhury, and T. Minka, "Precise indoor localization using PHY information," in *Proc. 9th ACM Int. Conf. Mobile Systems, Applications, and Services*, 2011, pp. 413–414.

[30] Z. H. Wu, Y. Han, Y. Chen, and K. J. R. Liu, "A time-reversal paradigm for indoor positioning system," *IEEE Trans. Veh. Technol.* (special section on Indoor

localization, tracking, and mapping with heterogeneous technologies), vol. 64, no. 4, pp. 1331–1339, Apr. 2015.

[31] C. Chen, Y. Han, Y. Chen, and K. J. R. Liu, “Indoor Global Positioning System with centimeter accuracy using Wi-Fi,” *IEEE Signal Process. Mag.*, vol. 33, no. 6, pp. 128–134, Nov. 2016.

[32] C. Chen, Y. Chen, Y. Han, H. Q. Lai, and K. J. R. Liu, “Achieving centimeter accuracy indoor localization on WiFi platforms: A frequency hopping approach,” *IEEE Internet Things J.*, vol. 4, no. 1, pp. 111–121, Feb. 2017.

[33] C. Chen, Y. Chen, Y. Han, H. Q. Lai, F. Zhang, and K. J. R. Liu, “Achieving centimeter accuracy indoor localization on WiFi platforms: A multi-antenna approach,” *IEEE Internet Things J.*, vol. 4, no. 1, pp. 122–134, Feb. 2017.

[34] F. Zhang, C. Chen, B. Wang, H. Q. Lai, and K. J. R. Liu, “A time-reversal spatial hardening effect for indoor speed estimation,” in *Proc. IEEE Int. Conf. Acoustics, Speech and Signal Processing*, New Orleans, Mar. 2017.

[35] F. Zhang, C. Chen, B. Wang, H. Q. Lai, and K. J. R. Liu, “WiBall: A time-reversal focusing ball method for indoor tracking,” unpublished, submitted to *IEEE Internet Things J.*, 2017.

[36] F. Zhang, C. Chen, B. Wang, H. Q. Lai, and K. J. R. Liu, “WiSpeed: A statistical electromagnetic approach for device-free indoor speed estimation,” submitted for publication.

[37] B. Wang, Y. Wu, F. Han, Y.-H. Yang, and K. J. R. Liu, “Green wireless communications: A time-reversal paradigm,” *IEEE J. Sel. Areas Commun.*, vol. 29, no. 8, pp. 1698–1710, Sept. 2011.

[38] Y. Jin, J. M. F. Moura, Y. Jiang, D. Stancil, and A. Cepni, “Time reversal detection in clutter: Additional experimental results,” *IEEE Trans. Aerosp. Electron. Syst.*, vol. 47, no. 1, pp. 140–154, Jan. 2011.

[39] J. M. F. Moura and Y. Jin, “Detection by time reversal: Single antenna,” *IEEE Trans. Signal Process.*, vol. 55, no. 1, pp. 187–201, Jan. 2007.

[40] Y. Chen, F. Han, Y.-H. Yang, H. Ma, Y. Han, C. Jiang, H. Q. Lai, D. Claffey, et al., “Time-reversal wireless paradigm for green Internet of Things: An overview,” *IEEE Internet Things J.*, vol. 1, no. 1, pp. 81–98, 2014.

[41] G. Lerosee, J. de Rosny, A. Tourin, A. Derode, G. Montaldo, and M. Fink, “Time reversal of electromagnetic waves,” *Phys. Rev. Lett.*, vol. 92, May 2004. doi: 10.1103/PhysRevLett.92.193904.

[42] Y. Chen, B. Wang, Y. Han, H. Q. Lai, Z. Safar, and K. J. R. Liu, “Why time reversal for future 5G wireless?” *IEEE Signal Process. Mag.*, vol. 33, no. 2, pp. 17–26, Mar. 2016.

[43] Y. Han, Y. Chen, B. Wang, and K. J. R. Liu, “Time-reversal massive multipath effect: A single-antenna massive MIMO solution,” *IEEE Trans. Commun.*, vol. 64, no. 8, pp. 3382–3394, Aug. 2016.

[44] A. Goldsmith, *Wireless Communications*. New York: Cambridge Univ. Press, 2005.

[45] M. Abramowitz, *Handbook of Mathematical Functions, with Formulas, Graphs, and Mathematical Tables*. New York: Dover, 1974.

[46] R. Schmidt, “Multiple emitter location and signal parameter estimation,” *IEEE Trans. Antennas Propag.*, vol. 34, pp. 276–280, Mar. 1986.

[47] B. J. Frey and D. Dueck, “Clustering by passing messages between data points,” *Science*, vol. 315, 2007. doi: 10.1126/science.1136800.

[48] H. El-Sallabi, P. Kyritsi, A. Paulraj, and G. Papanicolaou, “Experimental investigation on time reversal precoding for space-time focusing in wireless communications,” *IEEE Trans. Instrum. Meas.*, vol. 59, no. 6, pp. 1537–1543, 2010.

[49] Q. Xu, C. Jiang, Y. Han, B. Wang, and K. J. R. Liu, “Waveforming: An overview with beamforming,” *Commun. Surveys Tuts.*, vol. 20, no. 1, pp. 132–149.

[50] C. Jiang, B. Wang, Y. Han, Z. H. Wu, and K. J. R. Liu, “Exploring spatial focusing effect for spectrum sharing and network association,” *IEEE Trans. Wireless Commun.*, vol. 16, no. 7, pp. 4216–4231, July 2017.

[51] A. Banerjee, D. Maas, M. Bocca, N. Patwari, and S. Kasera, “Violating privacy through walls by passive monitoring of radio windows,” in *Proc. 2014 ACM Conf. Security and Privacy in Wireless and Mobile Networks*, 2014, pp. 69–80.

[52] H. Abdelnasser, M. Youssef, and K. A. Harras, “WiGest: A ubiquitous WiFi-based Gesture Recognition System,” in *Proc. IEEE Int. Conf. Computer Communications*, 2015. doi: 10.1109/INFOCOM.2015.7218525.

[53] J. Xiao, K. Wu, Y. Yi, L. Wang, and L. Ni, “FIMD: Fine-grained device-free motion detection,” in *Proc. 18th IEEE Int. Conf. Parallel and Distributed Systems*, Dec. 2012, pp. 229–235.

[54] F. Adib and D. Katabi, “See through walls with WiFi!” in *Proc. ACM Special Interest Group Data Communications*, 2013, pp. 75–86.

[55] C. Han, K. Wu, Y. Wang, and L. Ni, “WiFall: Device-free fall detection by wireless networks,” in *Proc. IEEE Int. Conf. Computer Communications*, Apr. 2014, pp. 271–279.

[56] Y. Wang, J. Liu, Y. Chen, M. Gruteser, J. Yang, and H. Liu, “E-eyes: Device-free location-oriented activity identification using fine-grained WiFi signatures,” in

*Proc. 20th ACM Annu. Int. Conf. Mobile Computing and Networking*, 2014, pp. 617–628.

[57] W. Xi, J. Zhao, X.-Y. Li, K. Zhao, S. Tang, X. Liu, and Z. Jiang, “Electronic frog eye: Counting crowd using WiFi,” in *Proc. IEEE Int. Conf. Computer Communications*, Apr. 2014, pp. 361–369.

[58] W. Wang, A. X. Liu, M. Shahzad, K. Ling, and S. Lu, “Understanding and modeling of WiFi signal based human activity recognition,” in *Proc. 21st ACM Annu. Int. Conf. Mobile Computing and Networking*, 2015, pp. 65–76.

[59] Y. Yang and A. Fathy, “Design and implementation of a low-cost real-time ultra-wide band see-through-wall imaging radar system,” in *Proc. IEEE MTT-S Int. Microwave Symp. Dig.*, June 2007, pp. 1467–1470.

[60] F. Adib, Z. Kabelac, D. Katabi, and R. C. Miller, “3D tracking via body radio reflections,” in *Proc. 11th USENIX Symp. Networked Systems Design and Implementation*, Apr. 2014, pp. 317–329.

[61] Q. Xu, Y. Chen, B. Wang, and K. J. R. Liu, “TRIEDS: Wireless events detection through the wall,” *IEEE Internet Things J.*, vol. 4, no. 3, pp. 723–735, June 2017.

[62] Q. Xu, Z. Safar, Y. Han, B. Wang, and K. J. R. Liu, “Statistical learning over time-reversal space for indoor monitoring system,” *IEEE Internet Things J.*, vol. PP, no. 99, pp. 1–1, Jan. 2018.

[63] A. Jain, A. A. Ross, and K. Nandakumar, *Introduction to Biometrics*. New York: Springer-Verlag, 2011.

[64] A. K. Jain, K. Nandakumar, and A. Ross, “50 years of biometric research: Accomplishments, challenges, and opportunities,” *Patt. Recog. Lett.*, vol. 79, pp. 80–105, Aug. 2016.

[65] G. Melia, “Electromagnetic absorption by the human body from 1-15 GHz,” Ph.D. dissertation, Univ. York, U.K., 2013.

[66] P. Beckmann and A. Spizzichino, *The Scattering of Electromagnetic Waves from Rough Surfaces*. Norwood, MA: Artech House, 1987.

[67] S. Gabriel, R. Lau, and C. Gabriel, “The dielectric properties of biological tissues: II. Measurements in the frequency range 10 Hz to 20 GHz,” *Phys. Med. Biol.*, vol. 41, no. 11, pp. 2251–2269, 1996.

[68] S. Gabriel, R. Lau, and C. Gabriel, “The dielectric properties of biological tissues: III. Parametric models for the dielectric spectrum of tissues,” *Phys. Med. Biol.*, vol. 41, no. 11, pp. 2271–2293, 1996.

[69] S. Levy, G. Sutton, P. C. Ng, L. Feuk, A. L. Halpern, B. P. Walenz, N. Axelrod, J. Huang, et al., “The diploid genome sequence of an individual human,” *PLoS Biol.*, vol. 5, no. 10, 2007. doi: 10.1371/journal.pbio.0050254.

[70] F. Adib, C.-Y. Hsu, H. Mao, D. Katabi, and F. Durand, “Capturing the human figure through a wall,” *ACM Trans. Graph.*, vol. 34, no. 6, pp. 1–13, Oct. 2015.

[71] F. Adib, Z. Kabelac, and D. Katabi, “Multi-person localization via RF body reflections,” in *Proc. 12th USENIX Symp. Networked Systems Design and Implementation*, May 2015, pp. 279–292.

[72] K. Ohara, T. Maekawa, and Y. Matsushita, “Detecting state changes of indoor everyday objects using WiFi channel state information,” *Proc. ACM Interactive, Mobile, Wearable Ubiquitous Technologies*, vol. 1, no. 3, Sept. 2017. doi: 10.1145/3131898.

[73] D. Gafurov, “A survey of biometric gait recognition: Approaches, security and challenges,” in *Proc. Annu. Norwegian Computer Science Conf.*, 2007, pp. 19–21.

[74] D. Tahmouh and J. Silvius, “Radar micro-Doppler for long range front-view gait recognition,” in *Proc. IEEE 3rd Int. Conf. Biometrics: Theory, Applications, and Systems*, 2009, pp. 1–6.

[75] R. G. Raj, V. C. Chen, and R. Lipps, “Analysis of radar human gait signatures,” *IET Signal Process.*, vol. 4, no. 3, pp. 234–244, 2010.

[76] Q. Xu, Y. Chen, B. Wang, and K. J. R. Liu, “Radio biometrics: Human recognition through a wall,” *IEEE Trans. Inf. Forensics Security*, vol. 12, no. 5, pp. 1141–1155, May 2017.

[77] B.-K. Park, S. Yamada, O. Boric-Lubecke, and V. Lubecke, “Single-channel receiver limitations in Doppler radar measurements of periodic motion,” in *Proc. IEEE Radio and Wireless Symp.*, Jan. 2006, pp. 99–102.

[78] F. Adib, H. Mao, Z. Kabelac, D. Katabi, and R. C. Miller, “Smart homes that monitor breathing and heart rate,” in *Proc. 33rd Annu. ACM Conf. Human Factors Computing Systems*, 2015, pp. 837–846.

[79] H. Abdelnasser, K. A. Harras, and M. Youssef, “UbiBreathe: A ubiquitous non-invasive WiFi-based breathing estimator,” in *Proc. 16th ACM Int. Symp. Mobile Ad Hoc Networking and Computing*, 2015, pp. 277–286.

[80] J. Liu, Y. Wang, Y. Chen, J. Yang, X. Chen, and J. Cheng, “Tracking vital signs during sleep leveraging off-the-shelf WiFi,” in *Proc. 16th ACM Int. Symp. Mobile Ad Hoc Networking and Computing*, 2015, pp. 267–276.

[81] C. Chen, Y. Han, Y. Chen, F. Zhang, H. Q. Lai, B. Wang, and K. J. R. Liu, “TR-BREATH: Time-reversal breathing rate estimation and detection,” *IEEE Trans. Biomed. Eng.*, vol. 65, no. 3, pp. 489–501.

